

Parallel Complex Diffusion for Scalable Time Series Generation

Rongyao Cai*

Yuxi Wan*

Institute of Cyber-Systems
and Control
Zhejiang University
Hangzhou, China

Kexin Zhang[†]

Institute of Cyber-Systems
and Control
Zhejiang University
Hangzhou, China

Ming Jin[†]

School of Information and
Communication Technology
Griffith University
Brisbane, Australia

Zhiqiang Ge

School of Mathematics
Southeast University
Nanjing, China

Qingsong Wen

Squirrel Ai Learning
Bellevue, USA

Yong Liu

Institute of Cyber-Systems
and Control
Zhejiang University
Hangzhou, China

Abstract

Modeling long-range dependencies in time series generation poses a fundamental trade-off between representational capacity and computational efficiency. Traditional temporal diffusion models suffer from local entanglement and the $O(L^2)$ cost of attention mechanisms. We address these limitations by introducing **PaCoDi (Parallel Complex Diffusion)**, a spectral-native architecture that decouples generative modeling in the frequency domain. PaCoDi fundamentally alters the problem topology: the Fourier Transform acts as a diagonalizing operator, converting locally coupled temporal signals into globally decorrelated spectral components. Theoretically, we prove the *Quadrature Forward Diffusion* and *Conditional Reverse Factorization* theorem, demonstrating that the complex diffusion process can be split into independent real and imaginary branches. We bridge the gap between this decoupled theory and data reality using a **Mean Field Theory (MFT) approximation** reinforced by an **interactive correction mechanism**. Furthermore, we generalize this discrete DDPM to continuous-time Frequency SDEs, rigorously deriving the **Spectral Wiener Process** describe the differential spectral Brownian motion limit. Crucially, PaCoDi exploits the *Hermitian Symmetry* of real-valued signals to compress the sequence length by half, achieving a **50% reduction in attention FLOPs** without information loss. We further derive a rigorous **Heteroscedastic Loss** to handle the non-isotropic noise distribution on the compressed manifold. Extensive experiments show that PaCoDi outperforms existing baselines in both generation quality and inference speed, offering a theoretically grounded and computationally efficient solution for time series modeling.

*Both authors contributed equally to this research.

[†]Team Leaders.

Permission to make digital or hard copies of all or part of this work for personal or classroom use is granted without fee provided that copies are not made or distributed for profit or commercial advantage and that copies bear this notice and the full citation on the first page. Copyrights for components of this work owned by others than the author(s) must be honored. Abstracting with credit is permitted. To copy otherwise, or republish, to post on servers or to redistribute to lists, requires prior specific permission and/or a fee. Request permissions from permissions@acm.org.
Conference'17, Washington, DC, USA

© 2018 Copyright held by the owner/author(s). Publication rights licensed to ACM.
ACM ISBN 978-1-4503-XXXX-X/2018/06
<https://doi.org/XXXXXXX.XXXXXXX>

Keywords

Time Series, Frequency Diffusion, Computational Complexity

ACM Reference Format:

Rongyao Cai, Yuxi Wan, Kexin Zhang, Ming Jin, Zhiqiang Ge, Qingsong Wen, and Yong Liu. 2026. Parallel Complex Diffusion for Scalable Time Series Generation. In . ACM, New York, NY, USA, 25 pages. <https://doi.org/XXXXXXX.XXXXXXX>

1 Introduction

The landscape of generative modeling has been revolutionized by two powerful paradigms: Denoising Diffusion Probabilistic Models (DDPMs) [6] and Score-Based Generative Models (SGMs) [15]. Recent unifying works [9, 16] have rigorously established that these methods can be interpreted as discretizations of continuous-time Stochastic Differential Equations (SDEs), where data is progressively perturbed by Brownian motion and synthesized by reversing the stochastic flow. While this SDE framework provides a solid theoretical foundation in Euclidean space (*i.e.*, pixel or time domain), it encounters a fundamental bottleneck when scaling to high-dimensional signals: the *Curse of Entanglement*.

In the vanilla temporal or spatial manifold, data points are intrinsically coupled via dense local dependencies. A standard SDE operating in this space must exhaust significant representational capacity to disentangle these correlations, resulting in inefficient transport trajectories and the prohibitive $O(L^2)$ complexity inherent in global attention mechanisms. We posit that the limitations of current diffusion models stem not from the SDE formulation itself, but from the **topology of the manifold** upon which the diffusion process is defined.

Although recent attempts have sought to incorporate spectral biases [19], they remain largely heuristic and often fall into a "pseudo-frequency" paradigm. These methods typically utilize spectral properties merely as an auxiliary proxy for noise scheduling [21], thereby retaining the primary computational bottleneck in the temporal domain. Alternatively, others employ statistically naive formulations that treat complex-valued spectral coefficients as concatenated real channels [13, 22]. Such approaches overlook the *intrinsic statistical geometry of the complex manifold*, *i.e.*, the quadrature independence and spectral heteroscedasticity proved

in our work, resulting in biased generative flows or suboptimal structural coherence.

More recently, shifting the diffusion process entirely from the temporal manifold to spectral domain has gained significant theoretical traction. Crabbé et al. [2] provided a seminal formalization of this paradigm, proving that standard SDE-based diffusion in the time domain corresponds to a dual process in the frequency domain driven by mirrored Brownian motions. Similarly, Kim et al. [7] proposed Spectral Mean Flows, which embed sequence distributions into Hilbert spaces and utilize spectral decomposition to enhance tractability for longer sequences. Despite these foundations, existing spectral diffusion models [17] continue to suffer from significant limitations: they typically rely on a *Monolithic Backbone*, failing to leverage spectral independence for parallelization, and lack *Mathematical Legitimacy* in rigorously modeling the stochastic dynamics via neural network on the complex plane.

To fundamentally resolve these issues, we introduce PaCoDi (**Parallel Complex Diffusion**), a comprehensive theoretical framework that generalizes score-based generative modeling to the frequency domain. We propose that the Fourier transform should be viewed not merely as a feature extractor, but as a diagonalizing operator for stochastic process, converting the intractable entangled temporal diffusion into a tractable decoupled spectral counterpart.

Our theoretical formalism proceeds along a rigorous "Discrete-to-Continuous" trajectory. We first establish the Frequency DDPM incorporating heteroscedastic complex noise, from which we derive the **Conditional Reverse Factorization Theorem**. This theorem proves that, unlike in the time domain, the conditional reverse dynamics in the frequency domain naturally factorize into independent real and imaginary branches. Crucially, this theoretical guarantee legitimizes quadrature modeling, effectively evading the restrictive holomorphic constraints imposed on complex-valued differentiation, allowing for more flexible neural parameterizations.

To bridge this idealized decoupled theory with the reality of coupled data (e.g., phase coherence), we introduce a **Mean Field Theory (MFT)** approximation, reinforced by an **Interactive Correction Mechanism** that recovers cross-domain dependencies via a variational proxy. We further generalize the discrete framework to continuous-time SDEs by constructing a **Spectral Wiener Process** to describe the limiting spectral Brownian motion. From an efficiency perspective, this parallel framework explicitly exploits *Hermitian Symmetry*, reducing the computational complexity of nonlinear operator (e.g., 50% for attention block).

Our contributions establish a self-contained theoretical system:

- **Rigorous Frequency Diffusion Theory:** We establish a mathematically rigorous frequency diffusion framework, characterized by quadrature forward process and conditional reverse factorization exploiting the statistical orthogonality of heteroscedastic complex noise.
- **A Unified Frequency SDE Framework:** We generalize score-based modeling to the frequency manifold, unifying discrete DDPMs and continuous SDEs. By constructing the spectral Wiener process, we derive the governing Frequency SDEs and prove the mathematical equivalence between frequency and temporal diffusion in the continuous limit.
- **Theoretical Factorization & Variational Correction:** We propose a parallel quadrature architecture that bypasses holomorphic constraints of complex-valued networks. To bridge the gap between decoupled theory and actual coupled data, we introduce MFT approximation with interactive correction, ensuring theoretical rigor meets practical efficacy.
- **Universal Efficiency & Performance:** We exploit hermitian symmetry to compress the state space, achieving a 50% theoretical reduction in attention complexity. Furthermore, we evaluate the dominantly superior performance of PaCoDi in unconditional and conditional time series generation tasks against 4, 5 baselines across diverse metrics, respectively.

2 Temporal Diffusion Modeling

Diffusion models establish a generative framework by defining a forward diffusion process that incrementally transforms a data distribution into a tractable prior. For a time series sample $\mathbf{x} \in \mathbb{R}^L$ with length L , the forward process is constructed as a Markov chain in the temporal manifold.

2.1 Forward Temporal Transition

The diffusion process transitions the data $\mathbf{x}_0 \sim q(\mathbf{x})$ to a sequence of latent states $\{\mathbf{x}_t\}_{t=1}^T$. Each transition step t adds infinitesimal Gaussian noise according to the rule:

$$q(\mathbf{x}_t | \mathbf{x}_{t-1}) = \mathcal{N}(\mathbf{x}_t; \sqrt{1 - \beta_t} \mathbf{x}_{t-1}, \beta_t \mathbf{I}) \quad (1)$$

where $\beta_t \in (0, 1)$ denotes a pre-defined various schedule. This iterative corruption ensures that for a sufficiently large T , the terminal state \mathbf{x}_T converges to a standard isotropic Gaussian distribution.

2.2 Structural Properties of Temporal Manifold

A fundamental advantage of the Gaussian diffusion kernel is the closed-form expression of any intermediate state \mathbf{x}_t relative to the initial observation \mathbf{x}_0 .

Proposition 2.1. (Temporal Marginal Distribution). Let $\alpha_t = 1 - \beta_t$ and $\bar{\alpha}_t = \prod_{s=1}^t \alpha_s$ be the cumulative signal retention factors. The marginal distribution of the state at step t is given by:

$$q(\mathbf{x}_t | \mathbf{x}_0) = \mathcal{N}(\mathbf{x}_t; \sqrt{\bar{\alpha}_t} \mathbf{x}_0, (1 - \bar{\alpha}_t) \mathbf{I}) \quad (2)$$

Through the reparameterization trick, the temporal state \mathbf{x}_t is explicitly expressed as:

$$\mathbf{x}_t = \sqrt{\bar{\alpha}_t} \mathbf{x}_0 + \sqrt{1 - \bar{\alpha}_t} \boldsymbol{\epsilon}, \quad \boldsymbol{\epsilon} \sim \mathcal{N}(\mathbf{0}, \mathbf{I}) \quad (3)$$

where $\boldsymbol{\epsilon}$ is the standard Gaussian noise in the temporal domain.

While temporal diffusion effectively captures local dynamics, the *strong temporal entanglement* between timestamps necessitates the network to resolve complex joint dependencies, which often hinders the modeling efficiency for long-range structures.

We address this challenge by extending the diffusion process to the complex frequency manifold. Leveraging the *asymptotic statistical independence* of spectral components, this frequency-native approach enables a decoupled modeling of global patterns, thereby naturally simplifying the optimization landscape and enhancing the fidelity of generated structural dependencies.

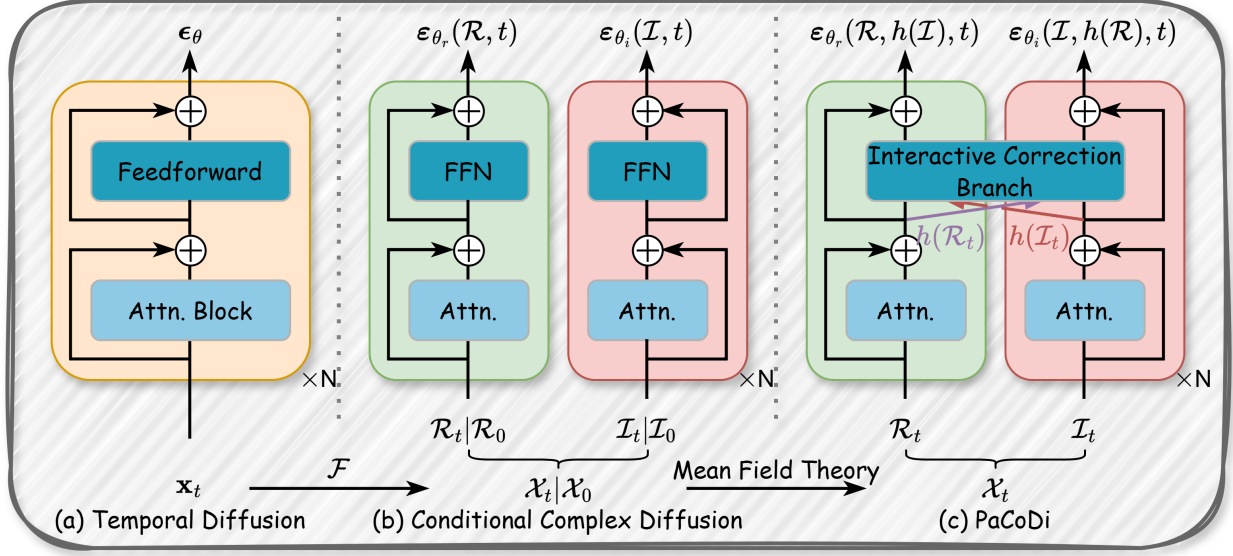


Figure 1: Architecture evolution from temporal to parallel complex diffusion. DiT blocks are visualized in a simplified form (Attn. and FFN only) for brevity. (a) Standard temporal diffusion. (b) Conditional complex diffusion with independent quadrature components under fixed conditional boundary \mathcal{X}_0 in frequency manifold. (c) PaCoDi: Our proposed framework that utilizes Interactive Correction Branch to recover correlation constraints marginalized by the Mean Field Theory (MFT) approximation.

3 Parallel Complex Diffusion Framework

3.1 Forward Diffusion in Complex Manifold

We initiate our framework by mapping the discrete-time diffusion process onto the frequency domain. Let $\mathbf{x}_t \in \mathbb{R}^L$ denote the temporal state at diffusion step t . We define the complex-valued state on the frequency manifold as $\mathcal{X}_t = \mathcal{F}(\mathbf{x}_t) = \mathcal{R}_t + j\mathcal{I}_t \in \mathbb{C}^L$, where $\mathcal{F}(\cdot)$ denotes the Discrete Fourier Transform (DFT).

By the linearity of the Fourier transform, the Gaussian transition kernel of the standard DDPM, $q(\mathbf{x}_t|\mathbf{x}_{t-1}) = \mathcal{N}(\mathbf{x}_t; \sqrt{1-\beta_t}\mathbf{x}_{t-1}, \beta_t\mathbf{I})$, induces an equivalent transition in the frequency domain:

$$\mathcal{X}_t = \sqrt{1-\beta_t}\mathcal{X}_{t-1} + \sqrt{\beta_t}\mathcal{E}_t \quad (4)$$

where $\mathcal{E}_t = \mathcal{F}(\epsilon_t)$ is the heteroscedastic spectral projection of the standard Gaussian noise $\epsilon_t \sim \mathcal{N}(\mathbf{0}, \sigma^2\mathbf{I})$, which we define as *Hermitian Complex Gaussian noise*. By Theorem A.1, the additivity of complex Gaussian noise holds the reparameterization of noise term. The tractability of parallelizing this diffusion process across the complex domain is fundamentally grounded in the statistical decoupling and well-defined heteroscedastic structure of \mathcal{E}_t .

Theorem 3.1. (Statistical Orthogonality of Complex Noise).

Let $\epsilon \sim \mathcal{N}(\mathbf{0}, \sigma^2\mathbf{I})$ be an isotropic Gaussian vector. Its spectral projection $\mathcal{E} = \mathcal{F}(\epsilon)$ decomposes into real and imaginary components $\epsilon_r = \Re(\mathcal{E})$ and $\epsilon_i = \Im(\mathcal{E})$. These components are statistically independent Gaussian vectors satisfying:

$$\text{Cov}(\epsilon_r, \epsilon_i) = \mathbf{0}_{L \times L}. \quad (5)$$

where $\epsilon_r \sim \mathcal{N}(\mathbf{0}, \Sigma_r)$ and $\epsilon_i \sim \mathcal{N}(\mathbf{0}, \Sigma_i)$. Specifically, Σ_r and Σ_i are heteroscedastic covariance matrices determined by frequency indices and Nyquist frequency.

Proof. See Appendix A.

Consequently, the joint density of complex noise factorizes as

$$p(\mathcal{E}) = p(\epsilon_r)p(\epsilon_i). \quad (6)$$

Leveraging Theorem 3.1, the complex-valued diffusion process in Eq. (4) losslessly decouples into two independent real-valued Markov chains. The marginal distribution at any diffusion step t can thus be expressed in closed form as:

$$\mathcal{R}_t = \sqrt{\bar{\alpha}_t}\mathcal{R}_0 + \sqrt{1-\bar{\alpha}_t}\epsilon_r, \quad \mathcal{I}_t = \sqrt{\bar{\alpha}_t}\mathcal{I}_0 + \sqrt{1-\bar{\alpha}_t}\epsilon_i \quad (7)$$

where $\bar{\alpha}_t = \prod_{s=1}^t (1-\beta_s)$ and $\epsilon_r \perp \epsilon_i$ are the cumulative noise from diffusion step 0 to t . This decoupling implies that $q(\mathcal{X}_t|\mathcal{X}_0) = q(\mathcal{R}_t|\mathcal{R}_0)q(\mathcal{I}_t|\mathcal{I}_0)$, allowing us to model the diffusion real and imaginary parts as parallel transport processes.

3.2 Conditional Factorization of Reverse Dynamics

The generative foundation of our PaCoDi framework requires ensuring that the quadrature components remain consistent during the denoising phase. While the marginal distribution $p(\mathcal{X}_t)$ is inevitably coupled due to the complex correlations in natural data \mathcal{X}_0 , the transitions conditioned on the data manifold exhibit a crucial independence property.

Proposition 3.2. (Conditional Reverse Factorization). Given the quadrature independence of the forward transition $q(\mathcal{X}_t|\mathcal{X}_{t-1})$ (Theorem 3.1), the reverse posterior distribution $q(\mathcal{X}_{t-1}|\mathcal{X}_t, \mathcal{X}_0)$ factorizes into two independent marginals when conditioned on a fixed initial boundary \mathcal{X}_0 :

$$q(\mathcal{X}_{t-1}|\mathcal{X}_t, \mathcal{X}_0) = q(\mathcal{R}_{t-1}|\mathcal{R}_t, \mathcal{R}_0) \cdot q(\mathcal{I}_{t-1}|\mathcal{I}_t, \mathcal{I}_0). \quad (8)$$

Proof. See Appendix B.

This proposition establishes the *structural orthogonality* of the complex diffusion mechanism. It implies that if we model the reverse transition using the standard variational bound, the Evidence Lower Bound (ELBO) theoretically splits into two independent terms.

However, unlike the standard temporal domain setting where noise is isotropic, the complex noise components $\epsilon_r \sim \mathcal{N}(\mathbf{0}, \Sigma_r)$ and $\epsilon_i \sim \mathcal{N}(\mathbf{0}, \Sigma_i)$ are governed by specific covariance structures (e.g., Hermitian symmetry). Thus, minimizing the variational bound corresponds to minimizing the Mahalanobis distance rather than the simple Euclidean norm (See Appendix D). Consequently, we can parameterize the denoising model using two neural networks optimized via a decoupled objective:

$$\begin{aligned} \min_{\theta} \mathbb{E}_{\mathcal{E}, t | \mathcal{X}_0} \left[\lambda_t \|\mathcal{E} - \mathcal{E}_{\theta}(\mathcal{X}, t)\|_{\Sigma^{-1}}^2 \right] &\iff \\ \min_{\theta_r, \theta_i} \underbrace{\mathbb{E}_{\epsilon_r, t | \mathcal{R}_0} \left[\lambda_t \|\epsilon_r - \epsilon_{\theta_r}(\mathcal{R}, t)\|_{\Sigma_r^{-1}}^2 \right]}_{\mathcal{L}_{\text{real}}^{\text{disc}}(\theta_r)} &+ \underbrace{\mathbb{E}_{\epsilon_i, t | \mathcal{I}_0} \left[\lambda_t \|\epsilon_i - \epsilon_{\theta_i}(\mathcal{I}, t)\|_{\Sigma_i^{-1}}^2 \right]}_{\mathcal{L}_{\text{imag}}^{\text{disc}}(\theta_i)} \end{aligned} \quad (9)$$

where $\|z\|_{\Sigma^{-1}}^2 = \mathbf{z}^\top \Sigma^{-1} \mathbf{z}$ denotes the squared Mahalanobis norm, and $\lambda_t = \frac{1-\alpha_t}{2\alpha_t(1-\alpha_t)}$ is the weighting term derived from the ELBO.

Eq. (9) presents an **idealized parallel diffusion framework**: the optimization of the real trajectory $\mathcal{L}_{\text{real}}^{\text{disc}}(\theta_r)$ and the imaginary trajectory $\mathcal{L}_{\text{imag}}^{\text{disc}}(\theta_i)$ are mathematically separable tasks conditioned on the known initial state \mathcal{X}_0 . Specifically, the real-part network θ_r takes only \mathcal{R}_t as input and is constrained only by the real noise component ϵ_r , and likewise for the imaginary part.

3.3 Parallel Modeling via Mean Field Theory

While the *true conditional posterior* $q(\mathcal{X}_{t-1} | \mathcal{X}_t, \mathcal{X}_0)$ is factorized (as proven in Proposition 3.2), the *generative transition* required for sampling, $p_{\theta}(\mathcal{X}_{t-1} | \mathcal{X}_t)$, must approximate the intractable marginal $q(\mathcal{X}_{t-1} | \mathcal{X}_t)$. Since $q(\mathcal{X}_{t-1} | \mathcal{X}_t)$ integrates over the coupled data prior $q(\mathcal{X}_0)$, it is inherently entangled (e.g., phase coherence in signal):

$$q(\mathcal{X}_{t-1} | \mathcal{X}_t) = \int q(\mathcal{X}_{t-1} | \mathcal{X}_t, \mathcal{X}_0) q(\mathcal{X}_0 | \mathcal{X}_t) d\mathcal{X}_0. \quad (10)$$

To reconcile the *computational efficiency* of parallel modeling with the statistical necessity of coupled modeling, we invoke the **Mean Field Theory (MFT) approximation**. We restrict the learnable generative model p_{θ} to a factorized variational family by assuming decoupled data distribution (Details in Appendix B.2):

$$p_{\theta}(\mathcal{X}_{t-1} | \mathcal{X}_t) \approx p_{\theta_r}(\mathcal{R}_{t-1} | \mathcal{R}_t) \cdot p_{\theta_i}(\mathcal{I}_{t-1} | \mathcal{I}_t). \quad (11)$$

By enforcing this factorization on the model architecture, we decompose the global optimization objective into two parallel streams.

However, the naive mean-field factorization in Eq. (11) discards the mutual dependencies required to recover phase information. To compensate for this information loss, we introduce an **Interactive Correction Mechanism** as a variational proxy. We modify the parameterization of the noise predictor such that each branch explicitly perceives its quadrature counterpart:

$$\mathcal{E}_{\theta}(\mathcal{X}, t) = \epsilon_{\theta_r}(\mathcal{R}, h(\mathcal{I}), t) + j\epsilon_{\theta_i}(\mathcal{I}, h(\mathcal{R}), t) \quad (12)$$

where $h(\cdot)$ is a projector of corresponding quadrature counterpart. In this design (illustrated in Figure 1), p_{θ} retains a *structurally*

decoupled parameterization allowing effective parallel inference, while its internal information flow remains coupled.

By combining the Mahalanobis distance metric derived in Eq. (9) with this interactive parameterization, we arrive at the final parallel training objective for PaCoDi:

$$\mathcal{L}_{\text{real}}^{\text{disc}}(\theta_r) = \mathbb{E}_{\mathcal{X}_0, \mathcal{E}, t} \left[\lambda_t \|\epsilon_{\theta_r}(\mathcal{R}, h(\mathcal{I}), t) - \epsilon_r\|_{\Sigma_r^{-1}}^2 \right], \quad (13)$$

$$\mathcal{L}_{\text{imag}}^{\text{disc}}(\theta_i) = \mathbb{E}_{\mathcal{X}_0, \mathcal{E}, t} \left[\lambda_t \|\epsilon_{\theta_i}(\mathcal{I}, h(\mathcal{R}), t) - \epsilon_i\|_{\Sigma_i^{-1}}^2 \right]. \quad (14)$$

3.4 Bypassing Holomorphic Constraints

Beyond computational benefits, our framework solves a critical theoretical conflict in complex-valued deep learning: *Holomorphicity vs. Expressivity*.

In native complex-valued networks, the noise predictor must satisfy the **Cauchy-Riemann Equations** $\left(\frac{\partial u}{\partial x} = \frac{\partial v}{\partial y}, \frac{\partial u}{\partial y} = -\frac{\partial v}{\partial x}\right)$ to be differentiable. This invokes *Liouville's Theorem*, which states that any bounded, entire function must be constant. This creates a fundamental dilemma: one cannot simultaneously achieve stability (boundedness) and non-linearity in a holomorphic setting.

PaCoDi circumvents this by formally decoupling the diffusion process from the constrained complex manifold \mathbb{C}^L to the unconstrained real vector space \mathbb{R}^{2L} (via Conditional Factorization). This topological shift legitimizes the use of powerful non-holomorphic activations (e.g., SiLU or GELU) within the parallel branches. Consequently, PaCoDi unlocks the full expressivity of modern deep learning to capture frequency features without violating mathematical consistency or resorting to heuristic approximations.

4 Continuous-time Perspective: Frequency SDEs

To provide a unified theoretical framework that encompasses our discrete PaCoDi theory, we extend the frequency diffusion process to a continuous-time Stochastic Differential Equation (SDE). This generalization allows us to leverage the powerful tools of stochastic calculus and ensures our method is mathematically grounded in the limit of infinite diffusion steps.

4.1 Forward SDE and Spectral Wiener Process

Consider the discrete transition rule $\mathcal{X}_{t+1} = \sqrt{1-\beta_t}\mathcal{X}_t + \sqrt{\beta_t}\mathcal{E}$. By deriving the continuum limit where $\Delta t \rightarrow 0$ and applying the Taylor expansion to the drift and diffusion coefficients (detailed derivation in Appendix E.1), the infinitesimal evolution of the frequency state converges to the following Itô SDE:

$$d\mathcal{X} = \underbrace{-\frac{1}{2}\beta(t)\mathcal{X}}_{\mathbf{f}(\mathcal{X}, t)} dt + \underbrace{\sqrt{\beta(t)}\mathbf{I}}_{\mathbf{g}(t)} d\mathcal{W} \quad (15)$$

where $\mathbf{f}(\cdot)$ and $\mathbf{g}(\cdot)$ denote the drift and diffusion coefficient vectors of a Variance Preserving (VP) SDE. The stochasticity is driven by the defined Spectral Wiener Process \mathcal{W} .

Definition 4.1. (Spectral Wiener Process). Let \mathbf{w} be a standard multi-dimensional Wiener process in the temporal domain. The **Spectral Wiener Process** \mathcal{W} is defined as the complex-valued process induced by the Fourier transform of \mathbf{w} :

$$\mathcal{W}_t := \mathcal{F}(\mathbf{w}_t). \quad (16)$$

Its differential increment, $d\mathcal{W} = d\mathbf{w}_r + jd\mathbf{w}_i$, is characterized by the following spectral properties:

- (1) **Complex Gaussianity:** The increments $d\mathbf{w}_r$ and $d\mathbf{w}_i$ are Gaussian random vectors with heteroscedastic covariance matrices $\Sigma_r dt$ and $\Sigma_i dt$, respectively.
- (2) **Quadrature Orthogonality:** The real and imaginary components are statistically independent, *i.e.*, $d\mathbf{w}_r \perp d\mathbf{w}_i$.

4.2 Bridging Complex Scores and Parallel Real-valued SDEs

To enable generation, we must reverse this continuous diffusion process. The reverse-time dynamics are governed by the gradient of the log-probability density, known as the score function.

4.2.1 Ideally Decoupled Reverse Dynamics. We first establish the theoretical form of the reverse SDE under ideal conditions. Utilizing *Wirtinger Calculus* for non-holomorphic functions, the complex score function decomposes linearly:

$$\nabla_{\bar{\mathcal{X}}} \log p_{t|0}(\mathcal{X}) = \frac{1}{2} (\nabla_{\mathcal{R}} \log p_{t|0}(\mathcal{X}) + j\nabla_{\mathcal{I}} \log p_{t|0}(\mathcal{X})) \quad (17)$$

where $p_{t|0}(\mathcal{X}) := p(\mathcal{X}_t | \mathcal{X}_0)$ is the conditional transition density.

Leveraging the conditional factorizability (Lemma C.1), for a fixed initial boundary \mathcal{X}_0 , the cross-terms in the log-density vanish, allowing the complex score to split into independent real and imaginary gradients (*i.e.*, $\nabla_{\mathcal{R}} \log p_{t|0}(\mathcal{X}) = \nabla_{\mathcal{R}} \log p_{t|0}(\mathcal{R})$). This leads to our main theorem on continuous-time parallelization.

Theorem 4.2. (Parallel Orthogonal Reverse SDE). Under the quadrature independence of the Spectral Wiener Process, the reverse-time SDE for a fixed initial condition \mathcal{X}_0 is given by:

$$d\mathcal{X} = [\mathbf{f}(\mathcal{X}, t) - \mathbf{g}(t)\mathbf{g}(t)^\top \nabla_{\bar{\mathcal{X}}} \log p_{t|0}(\mathcal{X})] dt + \mathbf{g}(t)d\hat{\mathcal{W}} \quad (18)$$

which naturally separates into two parallel real-valued SDEs:

$$\begin{cases} d\mathcal{R} = \left[\mathbf{f}(\mathcal{R}, t) - \frac{1}{2}\mathbf{g}(t)\mathbf{g}(t)^\top \nabla_{\mathcal{R}} \log p_{t|0}(\mathcal{R}) \right] dt + \mathbf{g}(t)d\hat{\mathbf{w}}_r \\ d\mathcal{I} = \left[\mathbf{f}(\mathcal{I}, t) - \frac{1}{2}\mathbf{g}(t)\mathbf{g}(t)^\top \nabla_{\mathcal{I}} \log p_{t|0}(\mathcal{I}) \right] dt + \mathbf{g}(t)d\hat{\mathbf{w}}_i \end{cases} \quad (19)$$

where $d\hat{\mathcal{W}} = d\hat{\mathbf{w}}_r + jd\hat{\mathbf{w}}_i$ is the increment of the inverse Spectral Wiener Process flowing backward in time.

Proof. See Appendix E.2.

4.2.2 MFT Approximation and Interactive Score Matching. While Theorem 4.2 guarantees decoupling for the conditional distribution $p_{t|0}(\mathcal{X})$, the practical generative process relies on the marginal score $\nabla_{\bar{\mathcal{X}}} \log p_t(\mathcal{X})$, which integrates over the data distribution $p(\mathcal{X}_0)$. Since natural signals exhibit strong phase coherence, $p(\mathcal{X}_0)$ is inherently coupled, rendering the true marginal score entangled.

To resolve the conflict between the decoupled SDE theory and the coupled data reality, we apply the MFT approximation (as motivated in Section 3.3) to continuous domain. We approximate the marginal score using the interactive correction branch estimator \mathcal{S}_θ :

$$\nabla_{\bar{\mathcal{X}}} \log p_t(\mathcal{X}) \approx \mathcal{S}_\theta(\mathcal{X}, t) = \frac{1}{2} (s_{\theta_r}(\mathcal{R}, h(\mathcal{I}), t) + js_{\theta_i}(\mathcal{I}, h(\mathcal{R}), t)). \quad (20)$$

This allows us to train the continuous-time model via Denoising Score Matching. Crucially, due to the spectral heteroscedasticity of complex noise, we derive the Score-Noise Identity (Appendix E.3) which relates the score to the noise via the precision matrix:

$$\nabla_{\mathcal{R}} \log p_{t|0}(\mathcal{R}) = -\frac{\Sigma_r^{-1}\boldsymbol{\varepsilon}_r}{\sqrt{1-\bar{\alpha}_t}}, \quad \nabla_{\mathcal{I}} \log p_{t|0}(\mathcal{I}) = -\frac{\Sigma_i^{-1}\boldsymbol{\varepsilon}_i}{\sqrt{1-\bar{\alpha}_t}} \quad (21)$$

where $\boldsymbol{\varepsilon}_r$ and $\boldsymbol{\varepsilon}_i$ denote the cumulative complex noise injected from diffusion step 0 to t .

Substituting this identity into the Fisher Divergence objective, we obtain the final continuous-time training objective, which mirrors the discrete case but with rigorous SDE grounding:

$$\mathcal{L}_{\text{real}}^{\text{cont}}(\theta_r) = \mathbb{E}_{\mathcal{X}_0, \boldsymbol{\varepsilon}, t} \left[\lambda(t) \left\| s_{\theta_r}(\mathcal{R}, h(\mathcal{I}), t) - \nabla_{\mathcal{R}} \log p_t(\mathcal{R}) \right\|_{\Sigma_r}^2 \right], \quad (22)$$

$$\mathcal{L}_{\text{imag}}^{\text{cont}}(\theta_i) = \mathbb{E}_{\mathcal{X}_0, \boldsymbol{\varepsilon}, t} \left[\lambda(t) \left\| s_{\theta_i}(\mathcal{I}, h(\mathcal{R}), t) - \nabla_{\mathcal{I}} \log p_t(\mathcal{I}) \right\|_{\Sigma_i}^2 \right] \quad (23)$$

where $\lambda(t) = \frac{1-\bar{\alpha}_t}{2\alpha_t}$ is the standard weighting term.

This formulation ensures that our parallel frequency SDEs converge to the true data distribution while respecting the statistical structure of the complex manifold. Furthermore, we establish the mathematical equivalence of the loss functions between the continuous and discrete formulations of PaCoDi in Appendix E.5.

5 Spectral-Native Optimization and Efficiency

Shifting the diffusion process to the frequency manifold fundamentally transforms the problem topology from a locally entangled temporal sequence to a globally decoupled spectral representation. We analyze this advantage from two perspectives: *Topological Simplification and Optimization Stability*.

5.1 Topological Simplification & Global Context

Orthogonal Decorrelation. Temporal modeling is burdened by the *local entanglement* of adjacent points due to autocorrelation. In contrast, the *Fourier Transform* acts as a natural **diagonalizing operator**, projecting the signal onto an orthogonal basis where spectral components \mathcal{X}_k become statistically independent. This effectively decomposes the intractable joint distribution $p(\mathbf{x}_{1:L})$ into simpler, nearly independent sub-problems $p(\mathcal{X}_k)$, significantly lowering the functional complexity the network must approximate.

Global Receptive Field by Design. Unlike temporal convolutions or attention mechanisms that rely on deep stacking to expand their receptive field, spectral features are linear combinations of the *entire* sequence. This grants PaCoDi a *global receptive field* at the very first layer, enabling the direct capture of global structural patterns regardless of sequence length, making the model remarkably efficient for long-range dependency modeling.

Layer Type	Temporal DiT (L)	PaCoDi ($2 \times L/2$)	Speedup Factor
Linear / MLP	$1 \times O(L)$	$2 \times O(L/2)$	1.0× (Iso-FLOPs)
Self-Attention	$1 \times O(L^2)$	$2 \times O(L^2/4)$	2.0× (50% Savings)
FFT Overhead	N/A	$2 \times O(L \log L)$	N/A

Table 1: Complexity Analysis. Comparison between Temporal DiT and PaCoDi. L denotes sequence length.

5.2 Unitary Isometry and Training Stability

The normalized DFT is a unitary linear operator $\mathcal{X} = \mathbf{U}\mathbf{x}$, satisfying $\mathbf{U}\mathbf{U}^H = \mathbf{I}$. This unitarity imparts two critical properties that ensure training robustness:

- **Loss Unbiasedness (Parseval’s Equivalence):** Since \mathbf{U} is an isometry, Euclidean distance is strictly preserved: $\|\mathbf{x} - \hat{\mathbf{x}}\|_2^2 = \|\mathbf{U}(\mathbf{x} - \hat{\mathbf{x}})\|_2^2 = \|\mathcal{X} - \hat{\mathcal{X}}\|_2^2$. This guarantees that minimizing the ELBO in the spectral domain is mathematically identical to minimizing it in the temporal domain.
- **Optimization Stability:** Unitary transformations preserve the spectral radius of the Hessian matrix. Consequently, PaCoDi inherits the well-studied optimization landscape of standard diffusion models, ensuring stable convergence without recalibrating the noise schedule β_t or learning rates.

5.3 Hermitian Symmetry and Compression

While unitarity ensures stability, the Hermitian Symmetry of real-valued signals enables significant state-space compression.

For a real vector $\mathbf{x} \in \mathbb{R}^L$, its spectrum satisfies $\mathcal{X}_k = \bar{\mathcal{X}}_{L-k}$. For a standard-normalized input where $\mathbb{E}[\mathbf{x}] = 0$, the DC component ($k = 0$) is strictly zero. By discarding the DC term and the redundant negative frequencies, we define the **Compressed Frequency State**:

$$\tilde{\mathcal{X}} = [\mathcal{X}_1, \dots, \mathcal{X}_K]^T \in \mathbb{C}^K, \quad \text{where } K = \lfloor L/2 \rfloor. \quad (24)$$

This reduction halves the modeling dimensionality. However, to maintain mathematical rigor, we must account for the shift in noise distribution on this compressed manifold:

$$\tilde{\epsilon}_{r,k} \sim \mathcal{N}\left(0, \frac{\sigma^2}{2}(1 + \delta_{k,L/2})\right), \quad \tilde{\epsilon}_{i,k} \sim \mathcal{N}\left(0, \frac{\sigma^2}{2}(1 - \delta_{k,L/2})\right). \quad (25)$$

5.4 Computational Acceleration: 50% Speedup

By combining the state compression ($L \rightarrow L/2$) with our decoupled parallel architecture, PaCoDi achieves a theoretical speedup of 50% for attention-based backbones (e.g., DiT [12]) compared to temporal diffusion. Notably, the cost of FFT/iFFT is asymptotically negligible.

1. Linear Layers (Iso-FLOPs): For linear projections (MLP, Conv), the complexity scales linearly with sequence length. Although we use two branches, each processes half the sequence length: $\text{Cost} \propto 2 \times (L/2) = L$. Thus, PaCoDi maintains the same parameter count and FLOPs as the baseline for linear operations.

2. Self-Attention (Quadratic Reduction): The bottleneck of DiT is the attention mechanism, which scales quadratically with sequence length $O(L^2)$. The reduction in effective sequence length triggers a nonlinear efficiency gain. Ultimately, PaCoDi reduces the total Attention FLOPs by **50%**. Unlike naive complex-valued networks (which require 4 real multiplications per complex operation and yield no speedup), our decoupled real-valued design fully

Datasets	Samples	Dims	Datasets	Samples	Dims
ETT	17420	7	Sines	10000	5
Stocks	3773	6	Air	9333	15

Table 2: Description of Unconditional Generation Datasets.

unlocks the efficiency potential of spectral compression.

$$\text{Temporal Attn.} = O(L^2 \cdot C) \quad (26)$$

$$\text{PaCoDi Attn.} = \underbrace{O\left(\left(\frac{L}{2}\right)^2 \cdot C\right)}_{\text{Real Branch}} + \underbrace{O\left(\left(\frac{L}{2}\right)^2 \cdot C\right)}_{\text{Imag Branch}} = \frac{1}{2}O(L^2 \cdot C). \quad (27)$$

6 Experiments

6.1 Datasets & Baselines

To comprehensively evaluate PaCoDi, we compared its performance against state-of-the-art models across both conditional and unconditional tasks.

Baselines. For conditional generation, we compare against three supervised models: T2S [4], Diffusion-TS [21], and TimeVAE [3]. Additionally, we evaluate two zero-shot Foundation Models to assess generalization: GPT-4o-mini [1] and Llama3.1-8b [5]. For unconditional generation, we select four representative baselines: Diffusion-TS, TimeVAE, TimeGAN [20], and Temporal DDPM [6].

Datasets. For the conditional task, we strictly adhere to the settings of T2S for single-channel fragment-level generation using ETTh1, ETTm1 [23], ECL [18], Exchange [8], and Air Quality [3]. For the unconditional task, we synthesize multivariate series on ETTh1, Stocks [3], Sines [21], and Air Quality (Details in Table 2).

6.2 Experimental Setting

Evaluation Metrics. We evaluate unconditional generation using four metrics: (1) **Discriminative Score** [20]: classification accuracy distinguishing real vs. synthetic data (lower is better); (2) **Predictive Score** [20]: downstream prediction error via Train-on-Synthetic-Test-on-Real (TSTR); (3) **Context-FID** [11]: Wasserstein distance of latent representations; and (4) **Correlational Score** [10]: Frobenius norm of cross-correlation matrix differences.

For conditional tasks, we report **MSE** and **WAPE** [14], defined as $\sum_{i \in \Omega} |y_i - \hat{y}_i| / \sum_{i \in \Omega} |y_i|$, measuring the normalized deviation from ground truth.

Experimental Details. For the conditional generation task, we adopt the configuration of T2S, where textual embeddings modulate the AdaLN coefficients of the DiT backbone across horizons $L \in \{24, 48, 96\}$. In the unconditional setting, we sample sequences from Gaussian noise with horizons $L \in \{24, 64, 128, 256\}$, consistent with the protocols established in Diffusion-TS.

Specifically, the interactive correction branch in PaCoDi is integrated within the feedforward block as cross-quadrature operator. This module processes the concatenated outputs from the parallel attention blocks, formulated as $\text{MLP}(\text{Concat}(\text{Attn.}(\mathcal{R}), \text{Attn.}(\mathcal{I})))$, to facilitate interaction between the real and imaginary branches.

Models	Cont.	Disc.	Diff-TS	TimeVAE	TimeGAN	DDPM	
C-FID	ETTh1	0.202	<u>0.215</u>	0.927	0.899	15.771	0.556
	Stocks	<u>0.272</u>	0.209	0.436	0.343	2.989	0.636
	Sines	0.069	0.100	0.148	0.730	10.766	<u>0.071</u>
	Air	0.339	0.520	<u>0.397</u>	1.413	13.452	0.603
Corr.	ETTh1	0.041	0.049	0.086	0.072	1.440	<u>0.042</u>
	Stocks	<u>0.011</u>	0.008	0.013	0.087	0.355	<u>0.011</u>
	Sines	0.019	<u>0.021</u>	0.030	0.086	0.489	<u>0.021</u>
	Air	<u>0.135</u>	0.128	0.195	0.304	0.762	0.234
Discr.	ETTh1	0.074	<u>0.087</u>	0.136	0.176	0.438	0.138
	Stocks	<u>0.066</u>	0.061	0.106	0.129	0.342	0.195
	Sines	0.014	<u>0.016</u>	0.077	0.068	0.259	0.017
	Air	0.205	0.280	0.158	0.421	0.424	<u>0.202</u>
Pred.	ETTh1	0.107	<u>0.112</u>	0.117	0.119	0.161	0.116
	Stocks	0.037	<u>0.038</u>	0.037	<u>0.038</u>	0.063	0.042
	Sines	0.205	<u>0.206</u>	0.208	0.249	0.230	<u>0.206</u>
	Air	0.020	0.022	<u>0.021</u>	0.028	0.242	0.022
1 st Count	11	<u>3</u>	2	0	0	0	
2 nd Count	3	7	2	1	0	<u>6</u>	

Table 3: Average Performance of Unconditional Generation across Horizon $L \in \{24, 64, 128, 256\}$. Cont. and Disc. are the symbol of PaCoDi SDE and DDPM variants, respectively. Bold and underline denote best and second best results.

6.3 Performance Analysis

We evaluate PaCoDi across two primary tasks: *unconditional synthesis* and *conditional generation*. The experimental results demonstrate that PaCoDi consistently achieves SOTA performance across diverse datasets and evaluation metrics.

Conditional Generation. Table 4 presents a comparative analysis of PaCoDi against specialized generative models (e.g., T2S, Diffusion-TS) and general-purpose LLMs (e.g., GPT-4o-mini, Llama 3.1-8b). The SDE and DDPM variants of PaCoDi exhibit clear dominance, securing the top performance in 19 and 14 evaluation categories, respectively. This superiority remains consistent across diverse signal dynamics, from highly periodic patterns (e.g., ETTh1, ECL) to stochastic volatility (e.g., Exchange). A pivotal advantage of our spectral manifold modeling is its performance stability relative to sequence length; unlike temporal models that suffer from dependency entanglement, PaCoDi scales gracefully. For instance, on ETTh1 ($L = 96$), PaCoDi SDE achieves an MSE of 0.013, outperforming Diffusion-TS (0.031) by a factor of 2.3x. Notably, while general-purpose LLMs struggle with numerical precision and high-frequency fluctuations, PaCoDi delivers more physically consistent and precise forecasts, demonstrating a native advantage in modeling low-level signal dynamics.

Unconditional Generation. Table 3 summarizes the average performance for unconditional synthesis on four datasets across multiple sequence horizons (Details in Appendix G). PaCoDi, including both its SDE (Cont.) and DDPM (Disc.) variants, exhibits a decisive margin of superiority over strong baselines such as Diffusion-TS, TimeVAE, and TimeGAN. Collectively, our variants secure 14 out of 16 first-place rankings, with the SDE variant alone achieving 11 champions. This consistent performance across diverse datasets underscores the model’s robustness in capturing the

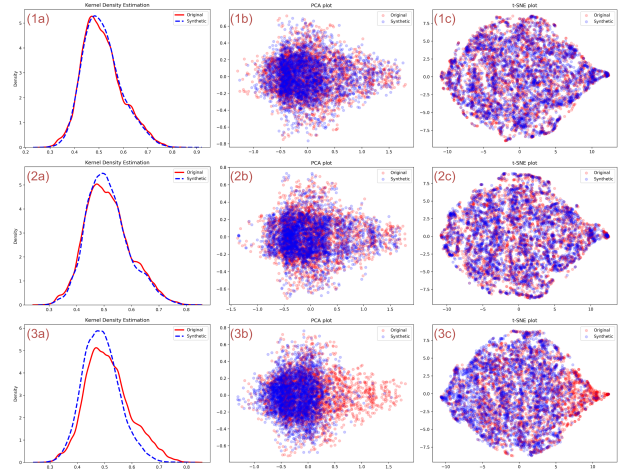


Figure 2: Data Distribution Visualization on ETTh1 ($L = 64$). Rows (1)–(3) correspond to PaCoDi DDPM, Diffusion-TS, and vanilla Diffusion. Columns (a)–(c) display Data Density Estimation, PCA, and t-SNE projections. Red and blue markers denote real and synthetic samples, respectively.

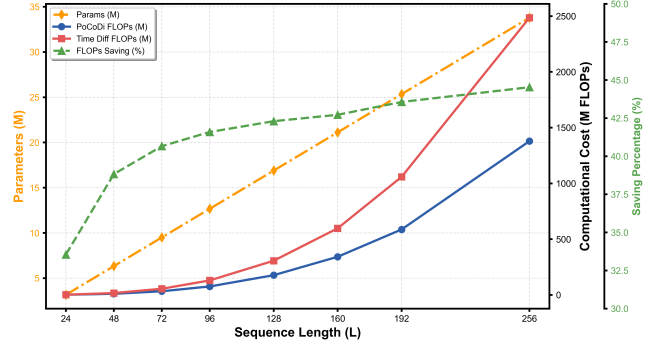


Figure 3: Computational Complexity Analysis

latent manifold of various temporal dynamics. A critical finding, validated by our results, is the stability of PaCoDi across the sequence horizon. For example, on ETTh1, while Diffusion-TS shows a performance degradation in Discriminative scores at $L = 256$, PaCoDi maintains high fidelity. This validates our theoretical claim that parallel quadrature decoupling effectively mitigates the "Curse of Entanglement" in long-horizon signals, allowing the model to resolve complex global dependencies.

Distribution Visualization. Furthermore, Figure 2 visualizes the data distribution on the ETTh1 dataset for unconditional synthesis. As evidenced by the results, the synthetic distribution of PaCoDi DDPM variant aligns more closely with the ground truth than those of Diffusion-TS and standard temporal-domain diffusion.

6.4 Computational Complexity Analysis

A primary advantage of PaCoDi is its significantly reduced computational overhead, achieved through the parallel modeling of quadrature components. To quantify this efficiency gain, we evaluate the computational complexity across sequence horizons ranging

Models	l	PaCoDi SDE		PaCoDi DDPM		T2S		Diffusion-TS		TimeVAE		GPT-4o-mini		Llama3.1-8b	
		WAPE	MSE	WAPE	MSE	WAPE	MSE	WAPE	MSE	WAPE	MSE	WAPE	MSE	WAPE	MSE
ETTh1	24	0.152	0.005	<u>0.163</u>	<u>0.006</u>	0.183	0.008	0.793	0.077	0.666	0.055	0.264	0.041	0.883	0.663
	48	0.163	0.005	<u>0.166</u>	<u>0.006</u>	0.234	0.013	1.207	0.120	0.647	0.055	0.414	0.080	0.923	1.260
	96	0.154	0.005	<u>0.155</u>	<u>0.006</u>	0.229	0.011	0.498	0.028	0.643	0.055	0.500	0.118	0.949	1.748
	Avg	0.156	0.005	<u>0.161</u>	<u>0.006</u>	0.215	0.011	0.833	0.075	0.652	0.055	0.393	0.080	0.918	1.224
ETTh1	24	0.169	0.008	<u>0.170</u>	0.008	0.426	0.033	0.604	0.040	0.666	0.048	0.244	<u>0.031</u>	1.134	0.798
	48	<u>0.196</u>	<u>0.010</u>	0.192	0.009	0.530	0.053	1.119	0.100	0.636	0.051	0.453	0.112	1.074	1.496
	96	0.228	0.013	<u>0.230</u>	0.013	0.414	0.041	0.546	<u>0.031</u>	0.664	0.057	0.706	0.395	1.079	1.761
	Avg	<u>0.198</u>	<u>0.010</u>	0.197	0.010	0.457	<u>0.042</u>	0.756	0.057	0.655	0.052	0.468	0.179	1.096	1.352
ECL	24	0.104	0.006	<u>0.109</u>	0.006	0.135	<u>0.010</u>	0.617	0.041	0.207	0.016	0.734	0.592	0.926	1.140
	48	0.135	0.010	0.135	0.010	<u>0.155</u>	<u>0.013</u>	1.128	0.102	0.208	0.017	1.014	1.065	1.038	1.416
	96	<u>0.155</u>	<u>0.013</u>	0.153	0.012	0.238	0.031	0.545	0.032	0.213	0.018	1.024	1.210	1.085	1.740
	Avg	0.131	<u>0.010</u>	<u>0.132</u>	0.009	0.176	0.018	0.763	0.058	0.209	0.017	0.924	0.956	1.016	1.432
Exchange	24	0.265	0.032	<u>0.266</u>	0.032	0.292	<u>0.033</u>	0.791	0.077	1.165	0.105	1.072	2.060	1.258	2.052
	48	0.254	<u>0.030</u>	0.254	0.029	<u>0.259</u>	0.033	1.217	0.122	1.064	0.106	0.933	1.074	1.562	2.125
	96	<u>0.237</u>	0.025	0.233	0.025	<u>0.480</u>	<u>0.047</u>	0.504	0.048	0.977	0.106	1.141	1.625	1.433	1.892
	Avg	<u>0.252</u>	0.029	0.251	0.029	0.344	<u>0.038</u>	0.837	0.082	1.069	0.106	1.049	1.586	1.418	2.023
Air Quality	24	<u>0.662</u>	0.013	0.699	<u>0.014</u>	0.884	0.020	0.806	0.078	2.303	0.022	0.557	0.379	0.878	0.697
	48	0.961	0.029	<u>0.824</u>	<u>0.028</u>	1.295	0.044	1.439	0.120	1.648	0.023	0.791	0.715	1.141	1.642
	96	<u>0.858</u>	<u>0.026</u>	0.915	0.030	1.377	0.049	0.508	0.028	1.270	0.024	0.928	1.127	1.085	1.551
	Avg	0.827	0.023	<u>0.813</u>	<u>0.024</u>	1.185	0.038	0.918	0.075	1.740	0.023	0.759	0.740	1.035	1.297
1 st Count	9	10	<u>5</u>	<u>9</u>	0	0	1	0	0	2	2	0	0	0	0
2 nd Count	<u>5</u>	<u>4</u>	8	5	2	<u>4</u>	0	1	0	0	0	1	0	0	0

Table 4: Conditional Generation. **Bold** and underline denote best and second best results.

from $L = 24$ to 256. Specifically, to maintain consistent model capacity, the hidden dimension h is scaled proportionally with the sequence horizon L . In this regime, the self-attention mechanism becomes the primary driver of the total computational cost as L increases. As illustrated in Figure 3, the computational cost for both PaCoDi and standard temporal diffusion grows quadratically ($O(L^2)$) relative to L . Notably, PaCoDi maintains a substantially lower cost profile; the FLOP savings ratio increases rapidly with L and asymptotically converges to 50%. This aligns with our theoretical expectation that bifurcating the attention block effectively bisects the quadratic scaling bottleneck of monolithic DiT.

6.5 Ablation Validation

We evaluate the impact of cross-quadrature interaction by comparing PaCoDi against a strictly decoupled spectral variant (Dec.) and a monolithic temporal baseline (Temp.) across continuous (SDE) and discrete (DDPM) frameworks.

The Necessity of Interactive Coupling. As evidenced in Table 5, while the Dec. benefits from parallel efficiency, it suffers from a severe collapse in generative fidelity, characterized by significant degradation in Context-FID and Discriminative scores. This performance gap empirically validates our theoretical hypothesis: treating quadrature components as entirely independent leads to the marginalization of essential phase-amplitude correlations. Notably, by incorporating the interactive correction branch, PaCoDi successfully recovers these vital dependencies, achieving superior fidelity that even surpasses the temporal baseline.

Robustness Across Manifolds. The performance gains are consistent across both discrete and continuous settings. PaCoDi

Models	DDPM			SDE			
	PaCoDi	Dec.	Temp.	PaCoDi	Dec.	Temp.	
Context-FID	24	<u>0.003\pm.001</u>	0.264 \pm .055	<u>0.038\pm.010</u>	<u>0.007\pm.001</u>	0.283 \pm .052	<u>0.228\pm.036</u>
	64	<u>0.018\pm.003</u>	1.573 \pm .177	<u>0.070\pm.023</u>	<u>0.012\pm.002</u>	1.621 \pm .277	<u>0.141\pm.010</u>
	128	<u>0.062\pm.005</u>	0.823 \pm .074	<u>0.163\pm.046</u>	<u>0.043\pm.002</u>	0.874 \pm .186	<u>0.162\pm.008</u>
	256	<u>0.317\pm.014</u>	0.883 \pm .134	<u>0.311\pm.321</u>	<u>0.213\pm.022</u>	1.081 \pm .083	<u>0.128\pm.011</u>
	Avg	0.100	0.886	<u>0.146</u>	0.069	0.965	<u>0.165</u>
Correlational	24	<u>0.019\pm.006</u>	<u>0.018\pm.007</u>	0.030 \pm .004	<u>0.026\pm.011</u>	<u>0.018\pm.006</u>	0.082 \pm .014
	64	0.030 \pm .010	<u>0.020\pm.007</u>	<u>0.019\pm.004</u>	<u>0.023\pm.007</u>	<u>0.025\pm.005</u>	0.030 \pm .012
	128	0.021 \pm .003	<u>0.015\pm.005</u>	<u>0.012\pm.007</u>	<u>0.017\pm.004</u>	0.020 \pm .003	<u>0.016\pm.003</u>
	256	<u>0.015\pm.004</u>	<u>0.015\pm.005</u>	<u>0.032\pm.008</u>	<u>0.011\pm.005</u>	<u>0.015\pm.007</u>	0.017 \pm .003
	Avg	<u>0.021</u>	0.017	0.023	0.019	<u>0.020</u>	0.036
Discriminative	24	<u>0.007\pm.008</u>	0.052 \pm .049	<u>0.019\pm.008</u>	<u>0.008\pm.004</u>	<u>0.035\pm.037</u>	0.136 \pm .198
	64	<u>0.010\pm.003</u>	0.136 \pm .038	<u>0.027\pm.041</u>	<u>0.008\pm.005</u>	0.156 \pm .083	<u>0.009\pm.007</u>
	128	<u>0.022\pm.007</u>	0.213 \pm .051	<u>0.011\pm.013</u>	<u>0.013\pm.016</u>	0.196 \pm .106	<u>0.041\pm.015</u>
	256	<u>0.023\pm.019</u>	0.183 \pm .070	<u>0.066\pm.142</u>	<u>0.027\pm.006</u>	0.194 \pm .096	<u>0.043\pm.029</u>
	Avg	0.016	0.146	<u>0.031</u>	0.014	0.145	<u>0.057</u>
Predictive	24	<u>0.093\pm.000</u>	<u>0.095\pm.000</u>	0.188 \pm .007	<u>0.093\pm.000</u>	<u>0.094\pm.000</u>	<u>0.093\pm.000</u>
	64	<u>0.191\pm.002</u>	<u>0.192\pm.003</u>	0.255 \pm .001	<u>0.188\pm.003</u>	0.195 \pm .003	<u>0.191\pm.002</u>
	128	<u>0.252\pm.003</u>	<u>0.260\pm.005</u>	0.288 \pm .003	<u>0.252\pm.003</u>	0.260 \pm .006	<u>0.253\pm.004</u>
	256	<u>0.287\pm.003</u>	0.291 \pm .004	<u>0.119\pm.001</u>	<u>0.286\pm.003</u>	0.290 \pm .001	<u>0.287\pm.003</u>
	Avg	0.206	<u>0.210</u>	0.213	0.205	0.210	<u>0.206</u>

Table 5: Ablation Experiments on Sines dataset. **Bold** and underline denote best and second best results.

secures the top rankings, demonstrating that our MFT compensation mechanism effectively maintains the coherence of real and

imaginary flows even under unknown data distributions, bridging the gap between computational scalability and generative integrity.

7 Conclusion

In this paper, we presented PaCoDi, a novel diffusion framework that transposes the generative process from the temporal manifold to complex spectral manifold. Moving beyond existing heuristic spectral approaches, we established a rigorous mathematical foundation by proving the legitimacy of frequency-domain diffusion through the lens of discrete DDPM and its continuous SDE limits. Our theoretical derivation revealed the Quadrature Independence inherent in unitary transformations, providing a principled justification for our parallel-branch architecture. By decoupling real and imaginary components into independent yet interactive streams, PaCoDi effectively bisects the sequence length for non-linear kernels, achieving a 50% reduction in the computational complexity of the self-attention mechanism. Extensive experiments across diverse benchmarks demonstrate that PaCoDi consistently achieves superior performance in both unconditional synthesis and conditional generation, effectively bridging the gap between computational scalability and generative fidelity.

References

- [1] Josh Achiam, Steven Adler, Sandhini Agarwal, Lama Ahmad, Ilge Akkaya, Florencia Leoni Aleman, Diogo Almeida, Janko Altmenschmidt, Sam Altman, Shyamal Anadkat, et al. 2023. GPT-4 technical report. *arXiv preprint arXiv:2303.08774* (2023).
- [2] Jonathan Crabbé, Nicolas Huynh, Jan Stanczuk, and Mihaela Van Der Schaar. 2024. Time series diffusion in the frequency domain. In *Proceedings of the 41st International Conference on Machine Learning (Vienna, Austria) (ICML'24)*. Article 374, 32 pages.
- [3] Abhyuday Desai, Cynthia Freeman, Zuhui Wang, and Ian Beaver. 2021. Timevae: A variational auto-encoder for multivariate time series generation. *arXiv preprint arXiv:2111.08095* (2021).
- [4] Yunfeng Ge, Jiawei Li, Yiji Zhao, Haomin Wen, Zhao Li, Meikang Qiu, Hongyan Li, Ming Jin, and Shirui Pan. 2025. T2S: High-resolution Time Series Generation with Text-to-Series Diffusion Models. In *Proceedings of the Thirty-Fourth International Joint Conference on Artificial Intelligence, IJCAI-25*, 5208–5216. Main Track.
- [5] Aaron Grattafiori, Abhimanyu Dubey, Abhinav Jauhri, Abhinav Pandey, Abhishek Kadian, Ahmad Al-Dahle, Aiesha Letman, Akhil Mathur, Alan Schelten, Alex Vaughan, et al. 2024. The llama 3 herd of models. *arXiv preprint arXiv:2407.21783* (2024).
- [6] Jonathan Ho, Ajay Jain, and Pieter Abbeel. 2020. Denoising Diffusion Probabilistic Models. In *Advances in Neural Information Processing Systems*, Vol. 33. Curran Associates, Inc., 6840–6851.
- [7] Jinwoo Kim, Max Beier, Petar Bevanda, Nayun Kim, and Seunghoon Hong. 2025. Sequence Modeling with Spectral Mean Flows. *arXiv preprint arXiv:2510.15366* (2025).
- [8] Guokun Lai, Wei-Cheng Chang, Yiming Yang, and Hanxiao Liu. 2018. Modeling Long- and Short-Term Temporal Patterns with Deep Neural Networks. In *The 41st International ACM SIGIR Conference on Research & Development in Information Retrieval (Ann Arbor, MI, USA) (SIGIR '18)*. 95–104.
- [9] Xu Liu, Taha Aksu, Juncheng Liu, Qingsong Wen, Yuxuan Liang, Caiming Xiong, Silvio Savarese, Doyen Sahoo, Junnan Li, and Chenghao Liu. 2025. Empowering Time Series Analysis with Synthetic Data: A Survey and Outlook in the Era of Foundation Models. *arXiv:2503.11411* [cs.LG]
- [10] Hao Ni, Lukasz Szpruch, Marc Sabate-Vidales, Baoren Xiao, Magnus Wiese, and Shujian Liao. 2022. Sig-wasserstein GANs for time series generation. In *Proceedings of the Second ACM International Conference on AI in Finance (ICAIF '21)*. Article 28, 8 pages.
- [11] Jéha Paul, Bohlke-Schneider Michael, Mercado Pedro, Kapoor Shubham, Singh Nirwan Rajbir, Flunkert Valentin, Gasthaus Jan, and Januschowski Tim. 2021. PSA-GAN: Progressive self attention gans for synthetic time series. *arXiv preprint arXiv:2108.00981* (2021).
- [12] William Peebles and Saining Xie. 2023. Scalable diffusion models with transformers. In *Proceedings of the IEEE/CVF international conference on computer vision*. 4195–4205.
- [13] Yurui Qian, Qi Cai, Yingwei Pan, Yehao Li, Ting Yao, Qibin Sun, and Tao Mei. 2024. Boosting Diffusion Models with Moving Average Sampling in Frequency Domain. In *Proceedings of the IEEE/CVF Conference on Computer Vision and Pattern Recognition (CVPR)*. 8911–8920.
- [14] Zezhi Shao, Fei Wang, Yongjun Xu, Wei Wei, Chengqing Yu, Zhao Zhang, Di Yao, Tao Sun, Guangyin Jin, Xin Cao, Gao Cong, Christian S. Jensen, and Xueqi Cheng. 2025. Exploring Progress in Multivariate Time Series Forecasting: Comprehensive Benchmarking and Heterogeneity Analysis. *IEEE Trans. on Knowl. and Data Eng.* 37, 1 (2025), 291–305.
- [15] Yang Song and Stefano Ermon. 2020. Improved Techniques for Training Score-Based Generative Models. In *Advances in Neural Information Processing Systems*, Vol. 33. 12438–12448.
- [16] Yang Song, Jascha Sohl-Dickstein, Diederik P Kingma, Abhishek Kumar, Stefano Ermon, and Ben Poole. 2021. Score-Based Generative Modeling through Stochastic Differential Equations. In *International Conference on Learning Representations*.
- [17] Haixin Wang, Jiashu Pan, Hao Wu, Fan Zhang, and Tailin Wu. 2025. FourierFlow: Frequency-aware Flow Matching for Generative Turbulence Modeling. *arXiv preprint arXiv:2506.00862* (2025).
- [18] Haixu Wu, Jiehui Xu, Jianmin Wang, and Mingsheng Long. 2021. Autoformer: Decomposition Transformers with Auto-Correlation for Long-Term Series Forecasting. In *Advances in Neural Information Processing Systems*, Vol. 34. 22419–22430.
- [19] Yiyuan Yang, Ming Jin, Haomin Wen, Chaoli Zhang, Yuxuan Liang, Lintao Ma, Yi Wang, Chenghao Liu, Bin Yang, Zenglin Xu, Shirui Pan, and Qingsong Wen. 2025. A Survey on Diffusion Models for Time Series and Spatio-Temporal Data. *ACM Comput. Surv.* (Dec. 2025).
- [20] Jinsung Yoon, Daniel Jarrett, and Mihaela van der Schaar. 2019. Time-series Generative Adversarial Networks. In *Advances in Neural Information Processing Systems*, Vol. 32.
- [21] Xinyu Yuan and Yan Qiao. 2024. Diffusion-TS: Interpretable Diffusion for General Time Series Generation. In *The Twelfth International Conference on Learning Representations*.
- [22] Chen Zhao, Weiling Cai, Chenyu Dong, and Chengwei Hu. 2024. Wavelet-based Fourier Information Interaction with Frequency Diffusion Adjustment for Underwater Image Restoration. In *Proceedings of the IEEE/CVF Conference on Computer Vision and Pattern Recognition (CVPR)*. 8281–8291.
- [23] Haoyi Zhou, Shanghang Zhang, Jieqi Peng, Shuai Zhang, Jianxin Li, Hui Xiong, and Wancai Zhang. 2021. Informer: Beyond Efficient Transformer for Long Sequence Time-Series Forecasting. *Proceedings of the AAAI Conference on Artificial Intelligence* 35, 12 (2021), 11106–11115.

A Statistical Property Derivation of Hermitian Complex Gaussian Noise

In this section, we rigorously derive the statistical properties of the spectral projection of i.i.d. temporal Gaussian noise, *i.e.*, *Hermitian Complex Gaussian Noise*. Let the temporal Gaussian noise vector be $\epsilon \in \mathbb{R}^L$ where $\epsilon \sim \mathcal{N}(\mathbf{0}, \sigma^2 \mathbf{I})$. We prove that its spectral counterpart $\mathcal{E} = \mathcal{F}(\epsilon) = \epsilon_r + j\epsilon_i$ satisfies:

- **Quadrature Independence:** The real and imaginary components, ϵ_r and ϵ_i , are statistically independent ($\text{Cov}(\epsilon_r, \epsilon_i) = \mathbf{0}$).
- **Spectral Heteroscedasticity:** Their marginal distributions are $\epsilon_r \sim \mathcal{N}(\mathbf{0}, \Sigma_r)$ and $\epsilon_i \sim \mathcal{N}(\mathbf{0}, \Sigma_i)$, where the covariance matrices exhibit structured sparsity due to Hermitian symmetry.

A.1 Notation and Preliminaries

Let $n \in [0, L-1]$ denote the discrete time index and $k \in [0, L-1]$ denote the frequency bin index. The Discrete Fourier Transform (DFT) of the noise vector ϵ is defined as:

$$\mathcal{E}_k = \frac{1}{\sqrt{L}} \sum_{n=0}^{L-1} \epsilon_n \exp\left(-j \frac{2\pi kn}{L}\right) = \epsilon_{r,k} + j\epsilon_{i,k}, \quad (28)$$

where the real and imaginary components are:

$$\epsilon_{r,k} = \frac{1}{\sqrt{L}} \sum_{n=0}^{L-1} \epsilon_n \cos\left(\frac{2\pi kn}{L}\right), \quad \epsilon_{i,k} = -\frac{1}{\sqrt{L}} \sum_{n=0}^{L-1} \epsilon_n \sin\left(\frac{2\pi kn}{L}\right). \quad (29)$$

Since ϵ_n is Gaussian and the DFT is a linear transformation, $\epsilon_{r,k}$ and $\epsilon_{i,k}$ are jointly Gaussian. We rely on the following orthogonality identities of trigonometric sums for $k, l \in [0, L-1]$ (Lemma F.2):

$$\sum_{n=0}^{L-1} \cos\left(\frac{2\pi An}{L}\right) = \begin{cases} L & \text{if } A \equiv 0 \pmod{L} \\ 0 & \text{otherwise} \end{cases} \quad (30)$$

where A represents combinations like $k+l$ or $k-l$.

A.2 Statistical Moments

A.2.1 First Moment (Mean). By the linearity of expectation:

$$\mathbb{E}[\epsilon_{r,k}] = \frac{1}{\sqrt{L}} \sum_{n=0}^{L-1} \underbrace{\mathbb{E}[\epsilon_n]}_0 \cos(\cdot) = 0, \quad \mathbb{E}[\epsilon_{i,k}] = -\frac{1}{\sqrt{L}} \sum_{n=0}^{L-1} \underbrace{\mathbb{E}[\epsilon_n]}_0 \sin(\cdot) = 0. \quad (31)$$

Thus, $\mu_r = \mu_i = \mathbf{0}$.

A.2.2 Cross-Covariance (Real vs. Imaginary). We analyze the covariance between the real part at frequency k and the imaginary part at frequency l by Lemma F.1:

$$\begin{aligned} \text{Cov}(\epsilon_{r,k}, \epsilon_{i,l}) &= \mathbb{E}\left[\left(\frac{1}{\sqrt{L}} \sum_{n=0}^{L-1} \epsilon_n \cos \frac{2\pi kn}{L}\right) \left(-\frac{1}{\sqrt{L}} \sum_{m=0}^{L-1} \epsilon_m \sin \frac{2\pi lm}{L}\right)\right] \\ &= -\frac{1}{L} \sum_{n=0}^{L-1} \sum_{m=0}^{L-1} \underbrace{\mathbb{E}[\epsilon_n \epsilon_m]}_{\sigma^2 \delta_{n,m}} \cos \frac{2\pi kn}{L} \sin \frac{2\pi lm}{L} \\ &= -\frac{\sigma^2}{L} \sum_{n=0}^{L-1} \cos \frac{2\pi kn}{L} \sin \frac{2\pi ln}{L} \\ &= -\frac{\sigma^2}{2L} \sum_{n=0}^{L-1} \left(\sin \frac{2\pi n(k+l)}{L} - \sin \frac{2\pi n(k-l)}{L}\right). \end{aligned} \quad (32)$$

For any integer A , $\sum_{n=0}^{L-1} \sin(2\pi An/L) = 0$. Therefore:

$$\text{Cov}(\epsilon_{r,k}, \epsilon_{i,l}) = 0, \quad \forall k, l. \quad (33)$$

This proves the **Quadrature Independence** of the diffusion process of real and imaginary branches.

A.2.3 Auto-Covariance (Real vs. Real).

$$\begin{aligned}
\text{Cov}(\boldsymbol{\varepsilon}_{r,k}, \boldsymbol{\varepsilon}_{r,l}) &= \mathbb{E} \left[\left(\frac{1}{\sqrt{L}} \sum_{n=0}^{L-1} \boldsymbol{\varepsilon}_n \cos \frac{2\pi kn}{L} \right) \left(\frac{1}{\sqrt{L}} \sum_{m=0}^{L-1} \boldsymbol{\varepsilon}_m \cos \frac{2\pi lm}{L} \right) \right] \\
&= \frac{1}{L} \sum_{n=0}^{L-1} \sum_{m=0}^{L-1} \underbrace{\mathbb{E} [\boldsymbol{\varepsilon}_n \boldsymbol{\varepsilon}_m]}_{\sigma^2 \delta_{n,m}} \cos \frac{2\pi kn}{L} \cos \frac{2\pi lm}{L} \\
&= \frac{\sigma^2}{L} \sum_{n=0}^{L-1} \cos \frac{2\pi kn}{L} \cos \frac{2\pi ln}{L} \\
&= \frac{\sigma^2}{2L} \sum_{n=0}^{L-1} \left(\cos \frac{2\pi n(k-l)}{L} + \cos \frac{2\pi n(k+l)}{L} \right).
\end{aligned} \tag{34}$$

Applying the identity in Eq. (30):

- Term 1 is non-zero (L) only if $k = l$ (diagonal).
- Term 2 is non-zero (L) only if $k + l = L$ or $k + l = 0$ (anti-diagonal/DC).

This yields the variance structure:

$$\text{Cov}(\boldsymbol{\varepsilon}_{r,k}, \boldsymbol{\varepsilon}_{r,l}) = \frac{\sigma^2}{2} \cdot \begin{cases} 2 & \text{if } k = l = 0 \text{ (DC) or } k = l = L/2 \text{ (Nyquist)} \\ 1 & \text{if } k = l \text{ (Diagonal) or } k + l = L \text{ (Anti-Diagonal)} \\ 0 & \text{otherwise.} \end{cases} \tag{35}$$

A.2.4 Auto-Covariance (Imaginary vs. Imaginary). Similarly:

$$\begin{aligned}
\text{Cov}(\boldsymbol{\varepsilon}_{i,k}, \boldsymbol{\varepsilon}_{i,l}) &= \mathbb{E} \left[\left(-\frac{1}{\sqrt{L}} \sum_{n=0}^{L-1} \boldsymbol{\varepsilon}_n \sin \frac{2\pi kn}{L} \right) \left(-\frac{1}{\sqrt{L}} \sum_{m=0}^{L-1} \boldsymbol{\varepsilon}_m \sin \frac{2\pi lm}{L} \right) \right] \\
&= \frac{1}{L} \sum_{n=0}^{L-1} \sum_{m=0}^{L-1} \mathbb{E} [\boldsymbol{\varepsilon}_n \boldsymbol{\varepsilon}_m] \sin \frac{2\pi kn}{L} \sin \frac{2\pi lm}{L} \\
&= \frac{\sigma^2}{L} \sum_{n=0}^{L-1} \sin \frac{2\pi kn}{L} \sin \frac{2\pi ln}{L} \\
&= \frac{\sigma^2}{2L} \sum_{n=0}^{L-1} \left(\cos \frac{2\pi n(k-l)}{L} - \cos \frac{2\pi n(k+l)}{L} \right).
\end{aligned} \tag{36}$$

This yields:

$$\text{Cov}(\boldsymbol{\varepsilon}_{i,k}, \boldsymbol{\varepsilon}_{i,l}) = \frac{\sigma^2}{2} \cdot \begin{cases} 0 & \text{if } k = l = 0 \text{ or } k = l = L/2 \text{ (Vanishing Imaginary)} \\ 1 & \text{if } k = l \text{ (Diagonal)} \\ -1 & \text{if } k + l = L \text{ (Anti-Diagonal)} \\ 0 & \text{otherwise.} \end{cases} \tag{37}$$

A.3 Covariance Matrix Visualization

The derived covariance structures Σ_r and Σ_i are sparse matrices characterized by an "X-shape" structure (Diagonal + Anti-Diagonal), reflecting the Hermitian symmetry.

For an even L , the covariance matrices Σ_r and Σ_i are:

$$\begin{aligned}
\Sigma_r &= \sigma^2 \begin{bmatrix} 1 & 0 & 0 & \cdots & 0 & \cdots & 0 & 0 \\ 0 & \frac{1}{2} & 0 & \cdots & 0 & \cdots & 0 & \frac{1}{2} \\ 0 & 0 & \ddots & & \vdots & & \ddots & 0 \\ \vdots & \vdots & & \ddots & & & & \vdots \\ 0 & 0 & \cdots & \frac{1}{2} & 0 & \frac{1}{2} & \cdots & 0 \\ \vdots & \vdots & & & \vdots & & & \vdots \\ 0 & 0 & \cdots & 0 & 1 & 0 & \cdots & 0 \\ \vdots & \vdots & & \frac{1}{2} & 0 & \frac{1}{2} & \cdots & \vdots \\ 0 & 0 & \ddots & & \vdots & & \ddots & 0 \\ 0 & \frac{1}{2} & 0 & \cdots & 0 & \cdots & 0 & \frac{1}{2} \end{bmatrix}_{L \times L}, & \Sigma_i &= \sigma^2 \begin{bmatrix} 0 & 0 & 0 & \cdots & 0 & \cdots & 0 & 0 \\ 0 & \frac{1}{2} & 0 & \cdots & 0 & \cdots & 0 & -\frac{1}{2} \\ 0 & 0 & \ddots & & \vdots & & \ddots & 0 \\ \vdots & \vdots & & \ddots & & & & \vdots \\ 0 & 0 & \cdots & \frac{1}{2} & 0 & -\frac{1}{2} & \cdots & 0 \\ \vdots & \vdots & & & \vdots & & & \vdots \\ 0 & 0 & \cdots & 0 & 0 & 0 & \cdots & 0 \\ \vdots & \vdots & & -\frac{1}{2} & 0 & \frac{1}{2} & \cdots & \vdots \\ 0 & 0 & \ddots & & \vdots & & \ddots & 0 \\ 0 & -\frac{1}{2} & 0 & \cdots & 0 & \cdots & 0 & \frac{1}{2} \end{bmatrix}_{L \times L}
\end{aligned} \tag{38}$$

For an odd L , the covariance matrices Σ_r and Σ_i are:

$$\Sigma_r = \sigma^2 \begin{bmatrix} 1 & 0 & 0 & \cdots & \cdots & 0 & 0 \\ 0 & \frac{1}{2} & 0 & \cdots & \cdots & 0 & \frac{1}{2} \\ 0 & 0 & \ddots & & & \ddots & 0 \\ \vdots & \vdots & & \frac{1}{2} & \frac{1}{2} & & \vdots \\ \vdots & \vdots & & \frac{1}{2} & \frac{1}{2} & & \vdots \\ 0 & 0 & \ddots & & & \ddots & 0 \\ 0 & \frac{1}{2} & 0 & \cdots & \cdots & 0 & \frac{1}{2} \end{bmatrix}_{L \times L}, \quad \Sigma_i = \sigma^2 \begin{bmatrix} 0 & 0 & 0 & \cdots & \cdots & 0 & 0 \\ 0 & \frac{1}{2} & 0 & \cdots & \cdots & 0 & -\frac{1}{2} \\ 0 & 0 & \ddots & & & \ddots & 0 \\ \vdots & \vdots & & \frac{1}{2} & -\frac{1}{2} & & \vdots \\ \vdots & \vdots & & -\frac{1}{2} & \frac{1}{2} & & \vdots \\ 0 & 0 & \ddots & & & \ddots & 0 \\ 0 & -\frac{1}{2} & 0 & \cdots & \cdots & 0 & \frac{1}{2} \end{bmatrix}_{L \times L} \quad (39)$$

A.4 Additivity and Unitary Invariance

In the standard DDPM, the forward process relies on the property that the linear combination of independent Gaussian variables remains Gaussian. This allows the marginal distribution at any diffusion step t to be collapsed into a single transition: $\mathbf{X}_t = \sqrt{\bar{\alpha}_t} \mathbf{X}_0 + \sqrt{1 - \bar{\alpha}_t} \boldsymbol{\epsilon}$. We hereby prove that this property strictly holds with the complex frequency manifold.

Theorem A.1. (Additivity and Unitary Invariance). Let $\boldsymbol{\epsilon}_1, \boldsymbol{\epsilon}_2, \dots, \boldsymbol{\epsilon}_t \in \mathbb{R}^L$ be a sequence of i.i.d. temporal Gaussian noise vectors such that $\boldsymbol{\epsilon}_t \sim \mathcal{N}(\mathbf{0}, \sigma^2 \mathbf{I})$. Let $\mathcal{E}_t = \mathcal{F}(\boldsymbol{\epsilon}_t)$ be their respective spectral projections via the normalized Discrete Fourier Transform (DFT). Then:

- **Distributional Homomorphism:** The spectral noise \mathcal{E}_t preserves the second-order statistical homogeneity of the temporal noise within the complex Gaussian space.
- **Additive Superposition:** Any weighted sum $a\mathcal{E}_1 + b\mathcal{E}_2$ is distributionally equivalent to a new sample $\sqrt{a^2 + b^2} \mathcal{E}^*$ drawn from the original spectral noise distribution, where $\mathcal{E}^* = \mathcal{F}(\boldsymbol{\epsilon}^*)$ and $\boldsymbol{\epsilon}^* \sim \mathcal{N}(\mathbf{0}, \sigma^2 \mathbf{I})$.

Proof.

1. *Preservation under Unitary Transformation:* The normalized DFT operator can be represented as a unitary matrix $\mathbf{U} \in \mathbb{C}^{L \times L}$ satisfying $\mathbf{U}\mathbf{U}^H = \mathbf{I}$. The probability density function of the isotropic temporal noise is given by $p(\boldsymbol{\epsilon}) \propto \exp(-\frac{1}{2} \|\boldsymbol{\epsilon}\|^2)$. Since the unitary transform is an isometry, it preserves the ℓ_2 -norm:

$$\|\mathcal{E}\|^2 = \|\mathbf{U}\boldsymbol{\epsilon}\|^2 = \boldsymbol{\epsilon}^H \mathbf{U}^H \mathbf{U} \boldsymbol{\epsilon} = \|\boldsymbol{\epsilon}\|^2 \quad (40)$$

The covariance matrix of the spectral noise is transformed as $\text{Cov}(\mathcal{E}) = \mathbf{U}(\sigma^2 \mathbf{I})\mathbf{U}^H = \sigma^2 \mathbf{I}$. Thus, \mathcal{E} remains a standard complex Gaussian variable, proving that the spectral manifold is a statistically complete mapping of the temporal Gaussian space.

2. *Linearity and Superposition:* Consider the noise aggregation step in the diffusion chain. In the temporal domain, we have the well-known property:

$$\sqrt{\alpha_t} \boldsymbol{\epsilon}_{t-1} + \sqrt{1 - \alpha_t} \boldsymbol{\epsilon}_t = \boldsymbol{\epsilon}^* \sim \mathcal{N}(\mathbf{0}, \sigma^2 \mathbf{I}) \quad (\text{given } \alpha_t + (1 - \alpha_t) = 1) \quad (41)$$

Applying the linear operator \mathcal{F} to both side:

$$\mathcal{F}(\sqrt{\alpha_t} \boldsymbol{\epsilon}_{t-1} + \sqrt{1 - \alpha_t} \boldsymbol{\epsilon}_t) = \sqrt{\alpha_t} \mathcal{F}(\boldsymbol{\epsilon}_{t-1}) + \sqrt{1 - \alpha_t} \mathcal{F}(\boldsymbol{\epsilon}_t) = \sqrt{\alpha_t} \mathcal{E}_{t-1} + \sqrt{1 - \alpha_t} \mathcal{E}_t \quad (42)$$

By linearity, the left-hand side equals $\mathcal{F}(\boldsymbol{\epsilon}^*) = \mathcal{E}^*$. Since $\boldsymbol{\epsilon}^*$ is a valid sample from the standard temporal Gaussian distribution, its spectral counterpart \mathcal{E}^* is necessarily a valid sample from the standard spectral Gaussian distribution.

3. *Induction to Arbitrary Diffusion Step t :* By induction, the cumulative noise at step t can be expressed as:

$$\mathcal{E}_{\text{cumulative}} = \sum_{t=1}^T w_t \mathcal{E}_t = \mathcal{F} \left(\sum_{t=1}^T w_t \boldsymbol{\epsilon}_t \right) \quad (43)$$

where $\sum_{t=1}^T w_t^2 = 1 - \bar{\alpha}_t$. The temporal additivity ensures $\sum_{t=1}^T w_t \boldsymbol{\epsilon}_t = \sqrt{1 - \bar{\alpha}_t} \boldsymbol{\epsilon}^* \sim \mathcal{N}(\mathbf{0}, (1 - \bar{\alpha}_t) \mathbf{I})$. Consequently:

$$\mathcal{E}_{\text{cumulative}} = \sqrt{1 - \bar{\alpha}_t} \mathcal{F}(\boldsymbol{\epsilon}^*) = \sqrt{1 - \bar{\alpha}_t} \mathcal{E}^* \quad (44)$$

where \mathcal{E}^* is a sample drawn from the identical spectral distribution.

Q.E.D.

B Proof of Proposition 3.2 (Conditional Reverse Factorization)

Proof.

The reverse denoising process in DDPM is governed in the posterior distribution $q(\mathcal{X}_{t-1}|\mathcal{X}_t, \mathcal{X}_0)$. According to **Bayes' Theorem**, this conditional density is expressed as:

$$q(\mathcal{X}_{t-1}|\mathcal{X}_t, \mathcal{X}_0) = \frac{q(\mathcal{X}_t|\mathcal{X}_{t-1}, \mathcal{X}_0)q(\mathcal{X}_{t-1}|\mathcal{X}_0)}{q(\mathcal{X}_t|\mathcal{X}_0)}. \quad (45)$$

By the **Markov property** of the forward diffusion, the transition term simplifies to $q(\mathcal{X}_t|\mathcal{X}_{t-1}, \mathcal{X}_0) = q(\mathcal{X}_t|\mathcal{X}_{t-1})$. The core of the factorization proof relies on demonstrating that every term on the RHS of Eq. (45) factorizes into real and imaginary components.

1. *Forward Transition $q(\mathcal{X}_t|\mathcal{X}_{t-1})$:* The forward diffusion step is defined as $\mathcal{X}_t = \sqrt{1 - \beta_t}\mathcal{X}_{t-1} + \sqrt{\beta_t}\mathcal{E}_t$. Since the complex noise $\mathcal{E} = \varepsilon_r + j\varepsilon_i$ possesses statistically independent quadrature components (Theorem 3.1), the transition density naturally splits:

$$q(\mathcal{X}_t|\mathcal{X}_{t-1}) = q(\mathcal{R}_t|\mathcal{R}_{t-1}) \cdot q(\mathcal{I}_t|\mathcal{I}_{t-1}). \quad (46)$$

2. *Conditional Marginal $q(\mathcal{X}_t|\mathcal{X}_0)$:* We must distinguish between the data correlation within $\mathcal{X}_0 = \mathcal{R}_0 + j\mathcal{I}_0$ and the stochastic evolution of the diffusion. When the boundary condition \mathcal{X}_0 is **fixed** (i.e., conditioned upon), the mean vector $\sqrt{\alpha_t}\mathcal{X}_0$ is a constant. The stochasticity is driven solely by the cumulative noise. As proven rigorously in Lemma C.1 (see below), this implies:

$$q(\mathcal{X}_t|\mathcal{X}_0) = q(\mathcal{R}_t|\mathcal{R}_0) \cdot q(\mathcal{I}_t|\mathcal{I}_0). \quad (47)$$

B.1 Factorization of the Posterior

Substituting these factorized kernels back into Bayes' Theorem Eq. (45):

$$\begin{aligned} q(\mathcal{X}_{t-1}|\mathcal{X}_t, \mathcal{X}_0) &= \frac{[q(\mathcal{R}_t|\mathcal{R}_{t-1})q(\mathcal{I}_t|\mathcal{I}_{t-1})][q(\mathcal{R}_{t-1}|\mathcal{R}_0)q(\mathcal{I}_{t-1}|\mathcal{I}_0)]}{[q(\mathcal{R}_t|\mathcal{R}_0)q(\mathcal{I}_t|\mathcal{I}_0)]} \\ &= \underbrace{\frac{q(\mathcal{R}_t|\mathcal{R}_{t-1})q(\mathcal{R}_{t-1}|\mathcal{R}_0)}{q(\mathcal{R}_t|\mathcal{R}_0)}}_{\text{Real Posterior}} \cdot \underbrace{\frac{q(\mathcal{I}_t|\mathcal{I}_{t-1})q(\mathcal{I}_{t-1}|\mathcal{I}_0)}{q(\mathcal{I}_t|\mathcal{I}_0)}}_{\text{Imaginary Posterior}}. \end{aligned} \quad (48)$$

Following the canonical derivation of DDPM, these terms precisely correspond to the independent marginal posterior distributions:

$$q(\mathcal{X}_{t-1}|\mathcal{X}_t, \mathcal{X}_0) = q(\mathcal{R}_{t-1}|\mathcal{R}_t, \mathcal{R}_0) \cdot q(\mathcal{I}_{t-1}|\mathcal{I}_t, \mathcal{I}_0). \quad (49)$$

Q.E.D.

B.2 Transition to Mean Field Approximation

It is crucial to note the distinction between the true posterior and the generative transition. While $q(\mathcal{X}_{t-1}|\mathcal{X}_t, \mathcal{X}_0)$ factorizes, the learned reverse transition $p_\theta(\mathcal{X}_{t-1}|\mathcal{X}_t)$ requires marginalizing over the unknown \mathcal{X}_0 :

$$q(\mathcal{X}_{t-1}|\mathcal{X}_t) = \int q(\mathcal{X}_{t-1}|\mathcal{X}_t, \mathcal{X}_0)q(\mathcal{X}_0|\mathcal{X}_t)d\mathcal{X}_0. \quad (50)$$

Since \mathcal{R}_0 and \mathcal{I}_0 are strongly coupled in the natural data manifold (e.g., phase-magnitude relationships), the term $q(\mathcal{X}_0|\mathcal{X}_t)$ does not factorize. Consequently, the marginal $q(\mathcal{X}_{t-1}|\mathcal{X}_t)$ is entangled.

This motivates the Mean Field Theory (MFT) applied in Section 3.3. By assuming a factorized variational proxy, we enforce the following structure:

$$\begin{aligned} p_\theta(\mathcal{X}_{t-1}|\mathcal{X}_t) &\approx \int [q(\mathcal{R}_{t-1}|\mathcal{R}_t, \mathcal{R}_0)q(\mathcal{I}_{t-1}|\mathcal{I}_t, \mathcal{I}_0)] \cdot [p_{\theta_r}(\mathcal{R}_0|\mathcal{R}_t)p_{\theta_i}(\mathcal{I}_0|\mathcal{I}_t)] d\mathcal{R}_0 d\mathcal{I}_0 \\ &= \left(\int q(\mathcal{R}_{t-1}|\mathcal{R}_t, \mathcal{R}_0)p_{\theta_r}(\mathcal{R}_0|\mathcal{R}_t)d\mathcal{R}_0 \right) \cdot \left(\int q(\mathcal{I}_{t-1}|\mathcal{I}_t, \mathcal{I}_0)p_{\theta_i}(\mathcal{I}_0|\mathcal{I}_t)d\mathcal{I}_0 \right) \\ &= p_{\theta_r}(\mathcal{R}_{t-1}|\mathcal{R}_t) \cdot p_{\theta_i}(\mathcal{I}_{t-1}|\mathcal{I}_t). \end{aligned} \quad (51)$$

This derivation theoretically justifies why we can train parallel branches while needing the **Interactive Correction Mechanism** to recover the cross-correlations lost in this approximation.

C Algebraic Proof of Conditional Factorizability

Lemma C.1. (Conditional Factorizability of Complex Trajectories). *Given the quadrature independence of complex frequency noise, the conditional distribution $p(\mathcal{X}_t|\mathcal{X}_0)$ factorizes into independent marginals of its real and imaginary parts for any fixed initial boundary \mathcal{X}_0 :*

$$p(\mathcal{X}_t|\mathcal{X}_0) = p(\mathcal{R}_t|\mathcal{R}_0)p(\mathcal{I}_t|\mathcal{I}_0). \quad (52)$$

Proof.

For a non-holomorphic complex signal $\mathcal{X}_t = \mathcal{R}_t + j\mathcal{I}_t \in \mathbb{C}^L$ where spectral heteroscedasticity exists (i.e., $\Sigma_t^{\mathcal{R}} \neq \Sigma_t^{\mathcal{I}}$), we represent the complex variable using its augmented real vector $\mathcal{X}_{\text{aug}} = [\mathcal{R}_t^\top, \mathcal{I}_t^\top]^\top \in \mathbb{R}^{2L}$. Under the PaCoDi framework, the conditional distribution follows a **Generalized Complex Gaussian Distribution** over this augmented space:

$$p(\mathcal{X}_t|\mathcal{X}_0) \sim \mathcal{N}(\boldsymbol{\mu}_{\text{aug}}, \boldsymbol{\Sigma}_{\text{aug}}), \quad \text{where} \quad \boldsymbol{\mu}_{\text{aug}} = \begin{bmatrix} \boldsymbol{\mu}_t^{\mathcal{R}} \\ \boldsymbol{\mu}_t^{\mathcal{I}} \end{bmatrix}, \quad \boldsymbol{\Sigma}_{\text{aug}} = \begin{bmatrix} \Sigma_t^{\mathcal{R}} & \Sigma_t^{\mathcal{R}\mathcal{I}} \\ \Sigma_t^{\mathcal{I}\mathcal{R}} & \Sigma_t^{\mathcal{I}} \end{bmatrix}. \quad (53)$$

where $\boldsymbol{\mu}_t^{\mathcal{R}}, \boldsymbol{\mu}_t^{\mathcal{I}} \in \mathbb{R}^L$ are the conditional mean, the block matrices in $\boldsymbol{\Sigma}_{\text{aug}} \in \mathbb{R}^{2L \times 2L}$ represent the quadrature covariances and cross-covariance structures. The off-diagonal blocks $\Sigma_t^{\mathcal{R}\mathcal{I}}$ represent the cross-covariance between real and imaginary channels.

Given a fixed initial state $\mathcal{X}_0 = \mathcal{R}_0 + j\mathcal{I}_0$, the diffusion state \mathcal{X}_t is obtained via the reparameterization trick:

$$\mathcal{R}_t = \sqrt{\bar{\alpha}_t} \mathcal{R}_0 + \sqrt{1 - \bar{\alpha}_t} \boldsymbol{\varepsilon}_r, \quad \boldsymbol{\varepsilon}_r \sim \mathcal{N}(\mathbf{0}, \boldsymbol{\Sigma}_r), \quad (54)$$

$$\mathcal{I}_t = \sqrt{\bar{\alpha}_t} \mathcal{I}_0 + \sqrt{1 - \bar{\alpha}_t} \boldsymbol{\varepsilon}_i, \quad \boldsymbol{\varepsilon}_i \sim \mathcal{N}(\mathbf{0}, \boldsymbol{\Sigma}_i). \quad (55)$$

Based on the Quadrature Independence (Theorem 3.1), the noise components are statistically independent, i.e., $\text{Cov}(\boldsymbol{\varepsilon}_r, \boldsymbol{\varepsilon}_i) = \mathbf{0}$. Consequently, the cross-covariance block in the augmented matrix vanishes:

$$\Sigma_t^{\mathcal{R}\mathcal{I}} = (1 - \bar{\alpha}_t) \text{Cov}(\boldsymbol{\varepsilon}_r, \boldsymbol{\varepsilon}_i) = \mathbf{0}. \quad (56)$$

Thus, the parameters for the augmented Gaussian simplify to a block-diagonal form:

$$\boldsymbol{\mu}_{\text{aug}} = \sqrt{\bar{\alpha}_t} \begin{bmatrix} \mathcal{R}_0 \\ \mathcal{I}_0 \end{bmatrix}, \quad \boldsymbol{\Sigma}_{\text{aug}} = \begin{bmatrix} (1 - \bar{\alpha}_t) \boldsymbol{\Sigma}_r & \mathbf{0} \\ \mathbf{0} & (1 - \bar{\alpha}_t) \boldsymbol{\Sigma}_i \end{bmatrix}. \quad (57)$$

Since $\boldsymbol{\Sigma}_{\text{aug}}$ is block-diagonal, its determinant and inverse decompose linearly:

$$\det(\boldsymbol{\Sigma}_{\text{aug}}) = \det(\boldsymbol{\Sigma}_r^{\mathcal{R}}) \det(\boldsymbol{\Sigma}_i^{\mathcal{I}}), \quad \boldsymbol{\Sigma}_{\text{aug}}^{-1} = \text{Diag} \left((\boldsymbol{\Sigma}_r^{\mathcal{R}})^{-1}, (\boldsymbol{\Sigma}_i^{\mathcal{I}})^{-1} \right). \quad (58)$$

Substituting these into the multivariate Gaussian PDF:

$$\begin{aligned} p(\mathcal{X}_t|\mathcal{X}_0) &= \frac{1}{\sqrt{(2\pi)^{2L} \det(\boldsymbol{\Sigma}_{\text{aug}})}} \exp \left(-\frac{1}{2} \left[(\mathcal{X}_{\text{aug}} - \boldsymbol{\mu}_{\text{aug}})^\top \boldsymbol{\Sigma}_{\text{aug}}^{-1} (\mathcal{X}_{\text{aug}} - \boldsymbol{\mu}_{\text{aug}}) \right] \right) \\ &= \frac{1}{\sqrt{(2\pi)^{2L} \det(\boldsymbol{\Sigma}_r^{\mathcal{R}}) \det(\boldsymbol{\Sigma}_i^{\mathcal{I}})}} \exp \left(-\frac{1}{2} \left[(\mathcal{R}_t - \boldsymbol{\mu}_t^{\mathcal{R}})^\top (\boldsymbol{\Sigma}_r^{\mathcal{R}})^{-1} (\mathcal{R}_t - \boldsymbol{\mu}_t^{\mathcal{R}}) + (\mathcal{I}_t - \boldsymbol{\mu}_t^{\mathcal{I}})^\top (\boldsymbol{\Sigma}_i^{\mathcal{I}})^{-1} (\mathcal{I}_t - \boldsymbol{\mu}_t^{\mathcal{I}}) \right] \right) \\ &= \prod_{\zeta \in \{\mathcal{R}, \mathcal{I}\}} \frac{1}{\sqrt{(2\pi)^L \det(\boldsymbol{\Sigma}_t^\zeta)}} \exp \left(-\frac{1}{2} (\zeta_t - \boldsymbol{\mu}_t^\zeta)^\top (\boldsymbol{\Sigma}_t^\zeta)^{-1} (\zeta_t - \boldsymbol{\mu}_t^\zeta) \right) \\ &= p(\mathcal{R}_t|\mathcal{R}_0) \cdot p(\mathcal{I}_t|\mathcal{I}_0) \end{aligned} \quad (59)$$

This confirms that under a fixed boundary condition, the joint conditional density is the product of independent quadrature marginals. Q.E.D.

D Derivation of the Reverse Dynamics under General Heteroscedastic Gaussian Noise

This section presents the derivation of the DDPM reverse process for multidimensional data $\mathbf{x} \in \mathbb{R}^d$ perturbed by general Gaussian noise $\epsilon \sim \mathcal{N}(\mathbf{0}, \Sigma)$, where $\Sigma \in \mathbb{R}^{d \times d}$ is an arbitrary symmetric positive definite covariance matrix. This formulation covers cases with both element-wise heteroscedasticity (diagonal Σ) and inter-variable correlations (non-diagonal Σ).

D.1 Bayesian Formulation of the Reverse Step

Using **Bayes' Theorem**, the reverse transition probability $p(\mathbf{x}_{t-1}|\mathbf{x}_t)$ conditioned on \mathbf{x}_0 is given by:

$$p(\mathbf{x}_{t-1}|\mathbf{x}_t, \mathbf{x}_0) = \frac{p(\mathbf{x}_t|\mathbf{x}_{t-1})p(\mathbf{x}_{t-1}|\mathbf{x}_0)}{p(\mathbf{x}_t|\mathbf{x}_0)}. \quad (60)$$

Recall the forward diffusion transitions defined by the schedule $\alpha_t = 1 - \beta_t$ and $\bar{\alpha}_t = \prod_{s=1}^t \alpha_s$:

$$p(\mathbf{x}_t|\mathbf{x}_{t-1}) = \mathcal{N}(\mathbf{x}_t; \sqrt{\alpha_t}\mathbf{x}_{t-1}, (1 - \alpha_t)\Sigma), \quad (61)$$

$$p(\mathbf{x}_t|\mathbf{x}_0) = \mathcal{N}(\mathbf{x}_t; \sqrt{\bar{\alpha}_t}\mathbf{x}_0, (1 - \bar{\alpha}_t)\Sigma). \quad (62)$$

Substituting these densities into the Bayes' rule ratio:

$$p(\mathbf{x}_{t-1}|\mathbf{x}_t, \mathbf{x}_0) \propto \exp\left(-\frac{1}{2}\left[(\mathbf{x}_t - \sqrt{\alpha_t}\mathbf{x}_{t-1})^\top \frac{\Sigma^{-1}}{1 - \alpha_t} (\mathbf{x}_t - \sqrt{\alpha_t}\mathbf{x}_{t-1}) + (\mathbf{x}_{t-1} - \sqrt{\bar{\alpha}_{t-1}}\mathbf{x}_0)^\top \frac{\Sigma^{-1}}{1 - \bar{\alpha}_{t-1}} (\mathbf{x}_{t-1} - \sqrt{\bar{\alpha}_{t-1}}\mathbf{x}_0) - C(\mathbf{x}_t, \mathbf{x}_0)\right]\right) \quad (63)$$

where $C(\mathbf{x}_t, \mathbf{x}_0)$ denotes terms independent of \mathbf{x}_{t-1} .

D.2 Completing the Square

To identify the mean $\tilde{\boldsymbol{\mu}}_t$ and covariance $\tilde{\Sigma}_t$ of the resulting Gaussian $q(\mathbf{x}_{t-1}|\mathbf{x}_t, \mathbf{x}_0)$, we collect all terms quadratic and linear in \mathbf{x}_{t-1} .

1. *The Precision Matrix (Inverse Covariance)*: Extracting the quadratic terms $\mathbf{x}_{t-1}^\top (\cdot) \mathbf{x}_{t-1}$:

$$\begin{aligned} \tilde{\Sigma}_t^{-1} &= \frac{\alpha_t}{1 - \alpha_t} \Sigma^{-1} + \frac{1}{1 - \bar{\alpha}_{t-1}} \Sigma^{-1} \\ &= \left(\frac{\alpha_t}{1 - \alpha_t} + \frac{1}{1 - \bar{\alpha}_{t-1}} \right) \Sigma^{-1} \\ &= \left(\frac{\alpha_t(1 - \bar{\alpha}_{t-1}) + (1 - \alpha_t)}{(1 - \alpha_t)(1 - \bar{\alpha}_{t-1})} \right) \Sigma^{-1} \\ &= \left(\frac{1 - \bar{\alpha}_t}{(1 - \alpha_t)(1 - \bar{\alpha}_{t-1})} \right) \Sigma^{-1}. \end{aligned} \quad (64)$$

Inverting this yields the reverse covariance:

$$\tilde{\Sigma}_t = \frac{(1 - \alpha_t)(1 - \bar{\alpha}_{t-1})}{1 - \bar{\alpha}_t} \Sigma. \quad (65)$$

This result confirms that the shape of the noise covariance Σ is preserved throughout the reverse process, merely scaled by a time-dependent scalar.

2. *The Mean Vector*: Extracting the linear terms $-2\tilde{\boldsymbol{\mu}}_t^\top \tilde{\Sigma}_t^{-1} \mathbf{x}_{t-1}$ involves the matrix Σ^{-1} :

$$\tilde{\boldsymbol{\mu}}_t^\top \tilde{\Sigma}_t^{-1} = \frac{\sqrt{\alpha_t}}{1 - \alpha_t} \mathbf{x}_t^\top \Sigma^{-1} + \frac{\sqrt{\bar{\alpha}_{t-1}}}{1 - \bar{\alpha}_{t-1}} \mathbf{x}_0^\top \Sigma^{-1}. \quad (66)$$

Multiplying from the right by $\tilde{\Sigma}_t$:

$$\begin{aligned} \tilde{\boldsymbol{\mu}}_t &= \tilde{\Sigma}_t \Sigma^{-1} \left(\frac{\sqrt{\alpha_t}}{1 - \alpha_t} \mathbf{x}_t + \frac{\sqrt{\bar{\alpha}_{t-1}}}{1 - \bar{\alpha}_{t-1}} \mathbf{x}_0 \right) \\ &= \left(\frac{(1 - \alpha_t)(1 - \bar{\alpha}_{t-1})}{1 - \bar{\alpha}_t} \Sigma \Sigma^{-1} \right) \left(\frac{\sqrt{\alpha_t}}{1 - \alpha_t} \mathbf{x}_t + \frac{\sqrt{\bar{\alpha}_{t-1}}}{1 - \bar{\alpha}_{t-1}} \mathbf{x}_0 \right) \\ &= \frac{\sqrt{\alpha_t}(1 - \bar{\alpha}_{t-1})}{1 - \bar{\alpha}_t} \mathbf{x}_t + \frac{\sqrt{\bar{\alpha}_{t-1}}(1 - \alpha_t)}{1 - \bar{\alpha}_t} \mathbf{x}_0. \end{aligned} \quad (67)$$

Substituting $\mathbf{x}_0 = \frac{1}{\sqrt{\bar{\alpha}_t}} (\mathbf{x}_t - \sqrt{1 - \bar{\alpha}_t} \epsilon)$ into the mean equation allows us to express it in terms of the cumulative noise ϵ :

$$\tilde{\boldsymbol{\mu}}_t(\mathbf{x}_t, \epsilon) = \frac{1}{\sqrt{\alpha_t}} \left(\mathbf{x}_t - \frac{1 - \alpha_t}{\sqrt{1 - \bar{\alpha}_t}} \epsilon \right). \quad (68)$$

Thus, the true posterior is:

$$q(\mathbf{x}_{t-1}|\mathbf{x}_t, \mathbf{x}_0) = \mathcal{N}\left(\mathbf{x}_{t-1}; \tilde{\boldsymbol{\mu}}_t(\mathbf{x}_t, \boldsymbol{\epsilon}), \tilde{\boldsymbol{\Sigma}}_t\right). \quad (69)$$

D.3 Optimization Objective

We approximate the true process using a learned model $p_\theta(\mathbf{x}_{t-1}|\mathbf{x}_t)$ that predicts the noise $\boldsymbol{\epsilon}_\theta(\mathbf{x}_t, t)$. The distribution is parameterized as:

$$p_\theta(\mathbf{x}_{t-1}|\mathbf{x}_t) = \mathcal{N}\left(\mathbf{x}_{t-1}; \tilde{\boldsymbol{\mu}}_t(\mathbf{x}_t, \boldsymbol{\epsilon}_\theta), \tilde{\boldsymbol{\Sigma}}_t\right). \quad (70)$$

The training objective minimizes the KL divergence between the true posterior and the parameterized reverse process. Since both are Gaussian with identical covariance $\tilde{\boldsymbol{\Sigma}}_t$, the KL divergence reduces to the Mahalanobis distance between their means:

$$\begin{aligned} \mathcal{L} &= \mathbb{E}_q [D_{\text{KL}}(q(\mathbf{x}_{t-1}|\mathbf{x}_t, \mathbf{x}_0) \parallel p_\theta(\mathbf{x}_{t-1}|\mathbf{x}_t))] \\ &= \mathbb{E}_q \left[\frac{1}{2} (\tilde{\boldsymbol{\mu}}_t(\boldsymbol{\epsilon}) - \tilde{\boldsymbol{\mu}}_t(\boldsymbol{\epsilon}_\theta))^\top \tilde{\boldsymbol{\Sigma}}_t^{-1} (\tilde{\boldsymbol{\mu}}_t(\boldsymbol{\epsilon}) - \tilde{\boldsymbol{\mu}}_t(\boldsymbol{\epsilon}_\theta)) \right]. \end{aligned} \quad (71)$$

Substituting the expressions for $\tilde{\boldsymbol{\mu}}_t$ difference and $\tilde{\boldsymbol{\Sigma}}_t^{-1}$:

$$\begin{aligned} \tilde{\boldsymbol{\mu}}_t(\boldsymbol{\epsilon}) - \tilde{\boldsymbol{\mu}}_t(\boldsymbol{\epsilon}_\theta) &= -\frac{1 - \alpha_t}{\sqrt{\alpha_t} \sqrt{1 - \bar{\alpha}_t}} (\boldsymbol{\epsilon} - \boldsymbol{\epsilon}_\theta) \\ \tilde{\boldsymbol{\Sigma}}_t^{-1} &= \left(\frac{1 - \bar{\alpha}_t}{(1 - \alpha_t)(1 - \bar{\alpha}_{t-1})} \right) \boldsymbol{\Sigma}^{-1}. \end{aligned} \quad (72)$$

The loss simplifies to:

$$\mathcal{L} = \lambda(t) \cdot (\boldsymbol{\epsilon} - \boldsymbol{\epsilon}_\theta)^\top \boldsymbol{\Sigma}^{-1} (\boldsymbol{\epsilon} - \boldsymbol{\epsilon}_\theta), \quad (73)$$

where $\lambda(t)$ is a scalar weighting term dependent on the diffusion schedule.

Ignoring the weighting factors, the core optimization problem minimizes the Mahalanobis norm of the noise prediction error:

$$\mathcal{L}_{\text{simple}} = \mathbb{E}_{\mathbf{x}_0, \boldsymbol{\epsilon}, t} \left[\|\boldsymbol{\epsilon} - \boldsymbol{\epsilon}_\theta(\mathbf{x}_t, t)\|_{\boldsymbol{\Sigma}^{-1}}^2 \right]. \quad (74)$$

This confirms that for any Gaussian noise process with a general covariance matrix $\boldsymbol{\Sigma}$ (whether diagonal or not), the optimal loss function corresponds to the squared error weighted by the precision matrix $\boldsymbol{\Sigma}^{-1}$. This effectively whitens the residuals during training.

E Construction of Frequency Stochastic Differential Equation Framework

E.1 Derivation of Frequency SDEs from Discrete DDPM

In this section, we rigorously demonstrate that the discrete-time forward process of the Frequency DDPM converges to a Variance Preserving (VP) Stochastic Differential Equation (SDE) in the limit of infinite time steps.

E.1.1 Discrete-Time Evolution with Time Scaling. Let the diffusion process be indexed by discrete steps $i \in \{0, 1, \dots, N\}$. To pass to the continuous limit, we embed these steps into a continuous time interval $t \in [0, 1]$. We define the time discretization interval as $\Delta t = 1/N$, such that $t_i = i\Delta t$.

The discrete noise schedule β_i corresponds to a continuous noise function $\beta(t)$ scaled by the time step:

$$\beta_i := \beta(t)\Delta t \quad (75)$$

Substituting this scaling into the standard DDPM transition rule:

$$\mathcal{X}_{t+\Delta t} = \sqrt{1 - \beta(t)\Delta t}\mathcal{X}_t + \sqrt{\beta(t)\Delta t}\mathcal{E} \quad (76)$$

where $\mathcal{X}_t \in \mathbb{C}^L$ is the frequency state and $\mathcal{E} = \epsilon_r + j\epsilon_i$ is the hermitian complex Gaussian noise satisfying $\epsilon_r \sim \mathcal{N}(\mathbf{0}, \Sigma_r)$ and $\epsilon_i \sim \mathcal{N}(\mathbf{0}, \Sigma_i)$.

We apply the *Taylor series expansion* to the drift coefficient $\sqrt{1 - \beta(t)\Delta t}$ around $\Delta t = 0$:

$$\sqrt{1 - \beta(t)\Delta t} = 1 - \frac{1}{2}\beta(t)\Delta t + \mathcal{O}((\Delta t)^2) \quad (77)$$

Substituting this approximation back into Eq. (76) and rearranging terms to isolate the state increment $\Delta\mathcal{X}_t = \mathcal{X}_{t+\Delta t} - \mathcal{X}_t$:

$$\begin{aligned} \mathcal{X}_{t+\Delta t} &\approx \left(1 - \frac{1}{2}\beta(t)\Delta t\right)\mathcal{X}_t + \sqrt{\beta(t)\Delta t}\mathcal{E} \\ \Delta\mathcal{X}_t &\approx -\frac{1}{2}\beta(t)\mathcal{X}_t\Delta t + \underbrace{\sqrt{\beta(t)\Delta t}\mathcal{E}}_{\Delta\mathcal{W}_t} \end{aligned} \quad (78)$$

E.1.2 Continuous-Time Extension and the Spectral Wiener Process. We construct a **Spectral Wiener Process** \mathcal{W} , defined in the complex frequency domain. Recall that the increment of a standard real-valued Wiener process \mathbf{w} over a time interval Δt is given by:

$$\Delta\mathbf{w} = \mathbf{w}_{t+\Delta t} - \mathbf{w}_t \sim \mathcal{N}(\mathbf{0}, \Delta t \cdot \sigma^2\mathbf{I}) \quad (79)$$

which can be expressed as $\Delta\mathbf{w} = \sqrt{\Delta t} \cdot \epsilon$, where $\epsilon \sim \mathcal{N}(\mathbf{0}, \sigma^2\mathbf{I})$ is standard Gaussian noise.

For the complex-valued noise in the frequency domain, we analogously define the increment of the Spectral Wiener Process $\Delta\mathcal{W}$ as:

$$\Delta\mathcal{W} = \sqrt{\Delta t} \cdot \mathcal{E} \quad (80)$$

where $\mathcal{E} = \epsilon_r + j\epsilon_i$ is a complex Gaussian noise vector, with ϵ_r and ϵ_i denoting real and imaginary Gaussian components, respectively. These are independently distributed such that:

$$\epsilon_r \sim \mathcal{N}(\mathbf{0}, \Sigma_r), \quad \epsilon_i \sim \mathcal{N}(\mathbf{0}, \Sigma_i) \quad (81)$$

where Σ_r and Σ_i are covariance matrices defined in Eqs. (38) and (39) with scaling parameter σ .

Thus, the increment $\Delta\mathcal{W}$ decomposes into:

$$\Delta\mathcal{W} = \epsilon_r\sqrt{\Delta t} + j\epsilon_i\sqrt{\Delta t} = \Delta\mathbf{w}_r + j\Delta\mathbf{w}_i \quad (82)$$

where $\Delta\mathbf{w}_r$ and $\Delta\mathbf{w}_i$ represent increments of two independent real-valued Wiener processes projected onto the frequency domain.

Taking the limit as $\Delta t \rightarrow 0$ (identifying Δt with the differential dt), we obtain the differential form:

$$d\mathcal{W} = d\mathbf{w}_r + jd\mathbf{w}_i \quad (83)$$

where $d\mathbf{w}_r$ and $d\mathbf{w}_i$ are the differentials of independent real-valued Wiener processes.

This Frequency Wiener Process is intrinsically linked to the time-domain Wiener process via the Fourier transform:

$$d\mathcal{W} = \mathcal{F}(d\mathbf{w}) \quad (84)$$

thereby establishing a conjugate relationship between time-domain and frequency-domain stochastic dynamics. This formulation provides a rigorous foundation for analyzing continuous-time stochastic systems in the frequency domain.

E.1.3 Forward Stochastic Differential Equation. Taking the infinitesimal limit $\Delta t \rightarrow 0$, the finite difference $\Delta\mathcal{X}$ converges to the differential $d\mathcal{X}$, Δt becomes dt , and $\Delta\mathcal{W}$ becomes $d\mathcal{W}$. The difference equation converges in distribution to the following Itô Stochastic Differential Equation:

$$d\mathcal{X} = \underbrace{-\frac{1}{2}\beta(t)\mathcal{X}}_{\mathbf{f}(\mathcal{X},t)} dt + \underbrace{\sqrt{\beta(t)}\mathbf{I}}_{\mathbf{g}(t)} d\mathcal{W} \quad (85)$$

Resulting Continuous Dynamics

The derived equation represents a Variance Preserving (VP) SDE on the complex manifold, characterized by:

- **Drift Coefficient:** $\mathbf{f}(\mathcal{X}, t) = -\frac{1}{2}\beta(t)\mathcal{X}$, which exerts a linear force pulling the data distribution towards the origin (zero mean).
- **Diffusion Coefficient:** $\mathbf{g}(t) = \sqrt{\beta(t)}\mathbf{I}$, which injects spectral noise to increase entropy.

This derivation confirms that our Frequency DDPM is a valid discretization of the continuous Frequency SDE framework presented in Section 4.

E.2 Derivation of Independent Parallel Reverse SDE

In this section, we derive the reverse-time stochastic dynamics and prove that, under the condition of factorized marginals, the complex reverse SDE naturally decouples into two parallel real-valued processes.

E.2.1 The General Reverse-Time SDE. According to the reverse-time diffusion theory extended to the complex domain, the evolution of the process backwards in time is governed by the following SDE:

$$d\mathcal{X} = [\mathbf{f}(\mathcal{X}, t) - \mathbf{g}(t)\mathbf{g}(t)^\top \nabla_{\mathcal{X}} \log p_t(\mathcal{X})] dt + \mathbf{g}(t)d\hat{\mathcal{W}} \quad (86)$$

where $d\hat{\mathcal{W}}$ denotes the increment of the *inverse Spectral Wiener process* flowing backward in time, and $\nabla_{\mathcal{X}} \log p_t(\mathcal{X})$ represents the *Stein score function* defined over the complex manifold.

E.2.2 Score Decomposition via Wirtinger Calculus. We focus on the conditional reverse process given a fixed initial state \mathcal{X}_0 . As proven in **Lemma C.1** (Appendix B), the conditional density factorizes due to quadrature independence:

$$p_{t|0}(\mathcal{X}) := p(\mathcal{X}_t | \mathcal{X}_0) = p_{t|0}(\mathcal{R})p_{t|0}(\mathcal{I}). \quad (87)$$

To compute the gradient of this factorized real-valued probability density with respect to the complex variable \mathcal{X}_t , we employ **Wirtinger Calculus**. The conjugate gradient operator is defined as $\nabla_{\mathcal{X}} := \frac{1}{2}(\nabla_{\mathcal{R}} + j\nabla_{\mathcal{I}})$. Applying this to the log-density:

$$\begin{aligned} \nabla_{\mathcal{X}} \log p_{t|0}(\mathcal{X}) &= \frac{1}{2} \left(\frac{\partial}{\partial \mathcal{R}} + j \frac{\partial}{\partial \mathcal{I}} \right) [\log p_{t|0}(\mathcal{R}) + \log p_{t|0}(\mathcal{I})] \\ &= \frac{1}{2} \left(\underbrace{\frac{\partial \log p_{t|0}(\mathcal{R})}{\partial \mathcal{R}}}_{\nabla_{\mathcal{R}} \log p_{t|0}(\mathcal{R})} + \underbrace{\frac{\partial \log p_{t|0}(\mathcal{I})}{\partial \mathcal{R}}}_0 + j \underbrace{\frac{\partial \log p_{t|0}(\mathcal{R})}{\partial \mathcal{I}}}_0 + j \underbrace{\frac{\partial \log p_{t|0}(\mathcal{I})}{\partial \mathcal{I}}}_{\nabla_{\mathcal{I}} \log p_{t|0}(\mathcal{I})} \right) \\ &= \frac{1}{2} (\nabla_{\mathcal{R}} \log p_{t|0}(\mathcal{R}) + j \nabla_{\mathcal{I}} \log p_{t|0}(\mathcal{I})). \end{aligned} \quad (88)$$

This derivation explicitly shows that the cross-terms vanish, and the factor $\frac{1}{2}$ emerges naturally from the complex derivative definition.

E.2.3 Decoupling of the SDE. Since the noise schedule $\beta(t)$ is real-valued, the linear drift coefficient $\mathbf{f}(\mathcal{X}, t) = -\frac{1}{2}\beta(t)\mathcal{X}_t$ satisfies the additive property:

$$\mathbf{f}(\mathcal{X}, t) = \mathbf{f}(\mathcal{R}, t) + j\mathbf{f}(\mathcal{I}, t). \quad (89)$$

Substituting the decomposed score (Eq. (88)), the drift (Eq. (89)), and the spectral Wiener differential $d\hat{\mathcal{W}} = d\hat{\mathbf{w}}_r + jd\hat{\mathbf{w}}_i$ into the general reverse SDE (Eq. (86)), we obtain:

$$d(\mathcal{R} + j\mathcal{I}) = \left[(\mathbf{f}(\mathcal{R}, t) + j\mathbf{f}(\mathcal{I}, t)) - \mathbf{g}(t)\mathbf{g}(t)^\top \frac{1}{2} (\nabla_{\mathcal{R}} \log p_{t|0}(\mathcal{R}) + j\nabla_{\mathcal{I}} \log p_{t|0}(\mathcal{I})) \right] dt + \mathbf{g}(t)(d\hat{\mathbf{w}}_r + jd\hat{\mathbf{w}}_i). \quad (90)$$

By grouping real and imaginary terms, the complex SDE separates into two autonomous real-valued systems:

$$\begin{cases} d\mathcal{R} = \left[\mathbf{f}(\mathcal{R}, t) - \frac{1}{2} \mathbf{g}(t) \mathbf{g}(t)^\top \nabla_{\mathcal{R}} \log p_{t|0}(\mathcal{R}) \right] dt + \mathbf{g}(t) d\hat{\mathbf{w}}_r \\ d\mathcal{I} = \left[\mathbf{f}(\mathcal{I}, t) - \frac{1}{2} \mathbf{g}(t) \mathbf{g}(t)^\top \nabla_{\mathcal{I}} \log p_{t|0}(\mathcal{I}) \right] dt + \mathbf{g}(t) d\hat{\mathbf{w}}_i \end{cases} \quad (91)$$

where $d\hat{\mathbf{w}}_r$ and $d\hat{\mathbf{w}}_i$ are independent real-valued heteroscedastic Brownian motions.

Notably, the resulting independent SDEs for \mathcal{R}_t and \mathcal{I}_t are consistent with the initial assumption of their independent evolution, thereby completing a self-consistent theoretical framework

Conclusion. This result proves **Theorem 4.2**. It demonstrates that the reverse generation process can be rigorously modeled as two parallel real-valued SDEs without cross-interference, provided that the score function factorizes. In practice, our interactive correction branch architecture approximates this factorized score while re-introducing necessary cross-domain information to account for the marginal entanglement of $p(\mathcal{X}_0)$.

E.3 Derivation of the Exact Heteroscedastic Score-Noise Identity

In this section, we establish the exact duality between the complex spectral score function and the cumulative noise under a fixed initial condition \mathcal{X}_0 . This derivation formally links the score matching objective (SDE) with the noise prediction objective (DDPM) in the frequency domain.

E.3.1 Exact Factorization of Conditional Quadrature Components. According to the quadrature independence of the forward transition (Theorem 3.1), the complex state at diffusion step t can be expressed via the reparameterization trick as:

$$\mathcal{R}_t = \sqrt{\bar{\alpha}_t} \mathcal{R}_0 + \sqrt{1 - \bar{\alpha}_t} \boldsymbol{\varepsilon}_r, \quad \mathcal{I}_t = \sqrt{\bar{\alpha}_t} \mathcal{I}_0 + \sqrt{1 - \bar{\alpha}_t} \boldsymbol{\varepsilon}_i \quad (92)$$

where $\boldsymbol{\varepsilon}_r$ and $\boldsymbol{\varepsilon}_i$ represent the *cumulative noise* injected from $t = 0$ to t . They follow the spectral Gaussian distributions derived in Appendix A:

$$\boldsymbol{\varepsilon}_r \sim \mathcal{N}(\mathbf{0}, \Sigma_r), \quad \boldsymbol{\varepsilon}_i \sim \mathcal{N}(\mathbf{0}, \Sigma_i). \quad (93)$$

Consequently, the conditional distribution of the real component follows a multivariate Gaussian:

$$\mathcal{R}_t | \mathcal{R}_0 \sim \mathcal{N}(\boldsymbol{\mu}_t^{\mathcal{R}}, \Sigma_t^{\mathcal{R}}), \quad \text{where } \boldsymbol{\mu}_t^{\mathcal{R}} = \sqrt{\bar{\alpha}_t} \mathcal{R}_0, \quad \Sigma_t^{\mathcal{R}} = (1 - \bar{\alpha}_t) \Sigma_r. \quad (94)$$

The corresponding conditional density function is:

$$p_{t|0}(\mathcal{R}) = \frac{1}{\sqrt{(2\pi)^L \det(\Sigma_t^{\mathcal{R}})}} \exp\left(-\frac{1}{2} (\mathcal{R}_t - \boldsymbol{\mu}_t^{\mathcal{R}})^\top (\Sigma_t^{\mathcal{R}})^{-1} (\mathcal{R}_t - \boldsymbol{\mu}_t^{\mathcal{R}})\right) \quad (95)$$

E.3.2 Derivation of Quadrature Score Functions. Taking the logarithm of the conditional density for the real component:

$$\begin{aligned} \log p_{t|0}(\mathcal{R}) &= -\frac{1}{2} (\mathcal{R}_t - \boldsymbol{\mu}_t^{\mathcal{R}})^\top (\Sigma_t^{\mathcal{R}})^{-1} (\mathcal{R}_t - \boldsymbol{\mu}_t^{\mathcal{R}}) + \text{Const} \\ &= -\frac{1}{2(1 - \bar{\alpha}_t)} (\mathcal{R}_t - \sqrt{\bar{\alpha}_t} \mathcal{R}_0)^\top \Sigma_r^{-1} (\mathcal{R}_t - \sqrt{\bar{\alpha}_t} \mathcal{R}_0) + \text{Const}. \end{aligned} \quad (96)$$

To find the score function $\nabla_{\mathcal{R}} \log p_{t|0}(\mathcal{R})$, we utilize the matrix calculus identity $\nabla_{\mathbf{x}} (\mathbf{x} - \mathbf{a})^\top \mathbf{A} (\mathbf{x} - \mathbf{a}) = (\mathbf{A} + \mathbf{A}^\top) (\mathbf{x} - \mathbf{a})$. Noting that the spectral covariance matrix Σ_r (and thus its inverse) is symmetric:

$$\begin{aligned} \nabla_{\mathcal{R}} \log p_{t|0}(\mathcal{R}) &= -\frac{1}{2(1 - \bar{\alpha}_t)} \left[\Sigma_r^{-1} + (\Sigma_r^{-1})^\top \right] (\mathcal{R}_t - \sqrt{\bar{\alpha}_t} \mathcal{R}_0) \\ &= -\frac{1}{1 - \bar{\alpha}_t} \Sigma_r^{-1} \underbrace{(\mathcal{R}_t - \sqrt{\bar{\alpha}_t} \mathcal{R}_0)}_{\sqrt{1 - \bar{\alpha}_t} \boldsymbol{\varepsilon}_r} \\ &= -\frac{\Sigma_r^{-1} \boldsymbol{\varepsilon}_r}{\sqrt{1 - \bar{\alpha}_t}}. \end{aligned} \quad (97)$$

By symmetry, the score function for the imaginary component is derived analogously:

$$\nabla_{\mathcal{I}} \log p_{t|0}(\mathcal{I}) = -\frac{\Sigma_i^{-1} \boldsymbol{\varepsilon}_i}{\sqrt{1 - \bar{\alpha}_t}}. \quad (98)$$

E.3.3 Complex Score Merger via Wirtinger Calculus. We now unify these real-valued results into the complex domain. The **Wirtinger derivative** (conjugate gradient) is defined as: $\nabla_{\bar{\mathcal{X}}} := \frac{1}{2} (\nabla_{\mathcal{R}} + j\nabla_{\mathcal{I}})$. Since the joint conditional density factorizes as $p_{t|0}(\mathcal{X}) = p_{t|0}(\mathcal{R})p_{t|0}(\mathcal{I})$, the log-density exhibits an exact additive structure:

$$\log p_{t|0}(\mathcal{X}) = \log p_{t|0}(\mathcal{R}) + \log p_{t|0}(\mathcal{I}). \quad (99)$$

Substituting the quadrature scores into the Wirtinger operator:

$$\begin{aligned} \nabla_{\bar{\mathcal{X}}} \log p_{t|0}(\mathcal{X}) &= \frac{1}{2} (\nabla_{\mathcal{R}} \log p_{t|0}(\mathcal{X}) + j\nabla_{\mathcal{I}} \log p_{t|0}(\mathcal{X})) \\ &= \frac{1}{2} (\nabla_{\mathcal{R}} \log p_{t|0}(\mathcal{R}) + j\nabla_{\mathcal{I}} \log p_{t|0}(\mathcal{I})) \\ &= \frac{1}{2} \left(-\frac{\Sigma_r^{-1} \boldsymbol{\varepsilon}_r}{\sqrt{1 - \bar{\alpha}_t}} - j \frac{\Sigma_i^{-1} \boldsymbol{\varepsilon}_i}{\sqrt{1 - \bar{\alpha}_t}} \right) \\ &= -\frac{\Sigma_r^{-1} \boldsymbol{\varepsilon}_r + j \Sigma_i^{-1} \boldsymbol{\varepsilon}_i}{2\sqrt{1 - \bar{\alpha}_t}}. \end{aligned} \quad (100)$$

Conclusion. This derivation confirms the Heteroscedastic Score-Noise Identity. It reveals that the complex score function is not merely the noise scaled by a scalar (as in standard homoscedastic DDPMs), but is the precision-weighted noise vector:

$$\nabla_{\bar{\mathcal{X}}} \log p_{t|0}(\mathcal{X}) \propto -(\Sigma_r^{-1} \boldsymbol{\varepsilon}_r + j \Sigma_i^{-1} \boldsymbol{\varepsilon}_i). \quad (101)$$

This explicitly justifies the use of the Mahalanobis distance (weighted by Σ) in our loss function to counterbalance the spectral heteroscedasticity Σ^{-1} , ensuring efficient and unbiased optimization.

E.4 Marginal Score Approximation via Mean Field Theory

While the conditional score identity derived in Appendix E.3 is exact for a fixed \mathcal{X}_0 , the generative process requires the *marginal score* $\nabla_{\bar{\mathcal{X}}} \log p_t(\mathcal{X})$, which marginalizes over the unknown data distribution $p(\mathcal{X}_0)$. This section theoretically justifies the factorization assumption used in our parallel architecture.

E.4.1 The Entanglement of Marginal Dynamics. The true marginal score involves an integral over the potentially entangled data manifold:

We start by expressing the marginal score as an expectation over the posterior. Using the identity $\nabla_{\bar{\mathcal{X}}} \log p_t(\mathcal{X}) = \frac{\nabla_{\bar{\mathcal{X}}} p_t(\mathcal{X})}{p_t(\mathcal{X})}$ and the integral definition $p_t(\mathcal{X}) = \int p_{t|0}(\mathcal{X}) p(\mathcal{X}_0) d\mathcal{X}_0$, we derive:

$$\begin{aligned} \nabla_{\bar{\mathcal{X}}} \log p_t(\mathcal{X}) &= \frac{1}{p_t(\mathcal{X})} \int \nabla_{\bar{\mathcal{X}}} p_{t|0}(\mathcal{X}) p(\mathcal{X}_0) d\mathcal{X}_0 \\ &= \frac{1}{p_t(\mathcal{X})} \int [p_{t|0}(\mathcal{X}) \nabla_{\bar{\mathcal{X}}} \log p_{t|0}(\mathcal{X})] p(\mathcal{X}_0) d\mathcal{X}_0 \\ &= \int [\nabla_{\bar{\mathcal{X}}} \log p_{t|0}(\mathcal{X})] \underbrace{\frac{p_{t|0}(\mathcal{X}) p(\mathcal{X}_0)}{p_t(\mathcal{X})}}_{p(\mathcal{X}_0|\mathcal{X}_t) \text{ (Posterior)}} d\mathcal{X}_0 \\ &= \mathbb{E}_{p(\mathcal{X}_0|\mathcal{X}_t)} [\nabla_{\bar{\mathcal{X}}} \log p_{t|0}(\mathcal{X})] \end{aligned} \quad (102)$$

Substituting the exact conditional score from Eq. (88) (Appendix E.2):

$$\nabla_{\bar{\mathcal{X}}} \log p_t(\mathcal{X}) = \frac{1}{2} \int [\nabla_{\mathcal{R}} \log p_{t|0}(\mathcal{R}) + j \nabla_{\mathcal{I}} \log p_{t|0}(\mathcal{I})] p(\mathcal{X}_0|\mathcal{X}_t) d\mathcal{X}_0 \quad (103)$$

The Coupling Problem: In real-world time series, the real and imaginary components of the data prior $p(\mathcal{X}_0)$ are strongly coupled (e.g., phase coherence). Consequently, the posterior $p(\mathcal{X}_0|\mathcal{X}_t)$ does not factorize, meaning the expectation in Eq. (103) entangles the real and imaginary gradients. The marginal score for the real part depends on the imaginary part, and vice versa.

E.4.2 MFT Variational Proxy. To bypass this representational rigidity and enable efficient parallel modeling, we invoke Mean Field Theory (MFT). We approximate the complex joint distribution using a factorized variational proxy. Specifically, we assume the data prior factorizes as $p(\mathcal{X}_0) \approx p(\mathcal{R}_0)p(\mathcal{I}_0)$.

Combining this with the exact conditional factorization $p(\mathcal{X}_t|\mathcal{X}_0) = p(\mathcal{R}_t|\mathcal{R}_0)p(\mathcal{I}_t|\mathcal{I}_0)$ (Lemma C.1), the joint distribution factorizes fully:

$$p(\mathcal{X}_t, \mathcal{X}_0) \approx [p(\mathcal{R}_t|\mathcal{R}_0)p(\mathcal{R}_0)] \cdot [p(\mathcal{I}_t|\mathcal{I}_0)p(\mathcal{I}_0)]. \quad (104)$$

This implies that the marginal density and the posterior also factorize:

$$p_t(\mathcal{X}) = \int p_{t|0}(\mathcal{X})p(\mathcal{X}_0)d\mathcal{X}_0 \approx \int p_{t|0}(\mathcal{R})p(\mathcal{R}_0)d\mathcal{R}_0 \cdot \int p_{t|0}(\mathcal{I})p(\mathcal{I}_0)d\mathcal{I}_0 = p_t(\mathcal{R})p_t(\mathcal{I}) \quad (105)$$

$$p(\mathcal{X}_0|\mathcal{X}_t) = \frac{p_{t|0}(\mathcal{X})p(\mathcal{X}_0)}{p_t(\mathcal{X})} \approx \frac{p_{t|0}(\mathcal{R})p(\mathcal{R}_0)}{p_t(\mathcal{R})} \cdot \frac{p_{t|0}(\mathcal{I})p(\mathcal{I}_0)}{p_t(\mathcal{I})} = p(\mathcal{R}_0|\mathcal{R}_t)p(\mathcal{I}_0|\mathcal{I}_t). \quad (106)$$

Applying this factorized posterior to the score equation:

$$\begin{aligned} \nabla_{\bar{\mathcal{X}}} \log p_t(\mathcal{X}) &\approx \frac{1}{2} \iint [\nabla_{\mathcal{R}} \log p_{t|0}(\mathcal{R}) + j\nabla_{\mathcal{I}} \log p_{t|0}(\mathcal{I})] p(\mathcal{R}_0|\mathcal{R}_t)p(\mathcal{I}_0|\mathcal{I}_t)d\mathcal{R}_0d\mathcal{I}_0 \\ &= \frac{1}{2} \left(\underbrace{\int [\nabla_{\mathcal{R}} \log p_{t|0}(\mathcal{R})]p(\mathcal{R}_0|\mathcal{R}_t)d\mathcal{R}_0}_{\mathbb{E}[\text{Real Score}]} \cdot \underbrace{\int p(\mathcal{I}_0|\mathcal{I}_t)d\mathcal{I}_0}_1 \right) \\ &\quad + \frac{j}{2} \left(\underbrace{\int [\nabla_{\mathcal{I}} \log p_{t|0}(\mathcal{I})]p(\mathcal{I}_0|\mathcal{I}_t)d\mathcal{I}_0}_{\mathbb{E}[\text{Imag Score}]} \cdot \underbrace{\int p(\mathcal{R}_0|\mathcal{R}_t)d\mathcal{R}_0}_1 \right) \\ &= \frac{1}{2} (\nabla_{\mathcal{R}} \log p_t(\mathcal{R}) + j\nabla_{\mathcal{I}} \log p_t(\mathcal{I})) \end{aligned} \quad (107)$$

where we utilized the identity $\int [\nabla_{\mathbf{x}} \log p(\mathbf{x}|\mathbf{z})]p(\mathbf{z}|\mathbf{x})d\mathbf{z} = \nabla_{\mathbf{x}} \log p(\mathbf{x})$.

E.4.3 Decoupling via Vanishing Cross-Gradients. Alternatively, we can view this from the perspective of the Wirtinger derivative acting on the factorized marginal $p_t(\mathcal{X}) \approx p_t(\mathcal{R})p_t(\mathcal{I})$. Expanding the Wirtinger operator:

$$\begin{aligned} \nabla_{\bar{\mathcal{X}}} \log p_t(\mathcal{X}) &\approx \nabla_{\bar{\mathcal{X}}} [\log p_t(\mathcal{R}) + \log p_t(\mathcal{I})] \\ &= \frac{1}{2} (\nabla_{\mathcal{R}} + j\nabla_{\mathcal{I}}) [\log p_t(\mathcal{R}) + \log p_t(\mathcal{I})] \\ &= \frac{1}{2} \left(\nabla_{\mathcal{R}} \log p_t(\mathcal{R}) + \underbrace{\nabla_{\mathcal{R}} \log p_t(\mathcal{I})}_0 + j \underbrace{\nabla_{\mathcal{I}} \log p_t(\mathcal{R})}_0 + j\nabla_{\mathcal{I}} \log p_t(\mathcal{I}) \right) \end{aligned} \quad (108)$$

Under the MFT assumption, the marginal density $p_t(\mathcal{I})$ has no functional dependence on the real coordinate \mathcal{R} , and vice versa, causing the cross-gradients to vanish. Thus, we arrive at the decoupled marginal score:

$$\nabla_{\bar{\mathcal{X}}} \log p_t(\mathcal{X}) \approx \frac{1}{2} (\nabla_{\mathcal{R}} \log p_t(\mathcal{R}) + j\nabla_{\mathcal{I}} \log p_t(\mathcal{I})) \quad (109)$$

This derivation justifies the use of independent loss functions for the real and imaginary branches in our parallel architecture. While this factorized objective enforces computational efficiency, the Interactive Parallel Branches introduced in PaCoDi serve as a correction mechanism to compensate for the information lost during this MFT approximation.

E.5 Equivalence of Loss Functions between DDPM and SDE

In this section, we provide a formal proof demonstrating that the continuous-time score-matching objective $\mathcal{L}^{\text{cont}}$ is equivalent to the heteroscedastic noise-prediction objective $\mathcal{L}^{\text{disc}}$ used in the discrete-time formulation of PaCoDi.

E.5.1 Theoretical Expansion. We start from the continuous score-matching loss for the real component, weighted by spectral covariance Σ_r :

$$\mathcal{L}_{\text{real}}^{\text{cont}}(\theta_r) = \mathbb{E}_{\mathcal{X}_0, \mathcal{E}, t} \left[\lambda(t) \|s_{\theta_r}(\mathcal{R}, h(\mathcal{I}), t) - \nabla_{\mathcal{R}} \log p_{t|0}(\mathcal{R})\|_{\Sigma_r}^2 \right]. \quad (110)$$

Expanding the Mahalanobis norm $\|v\|_{\Sigma}^2 = v^{\top} \Sigma v$ into its quadratic form:

$$\mathcal{L}_{\text{real}}^{\text{cont}}(\theta_r) = \mathbb{E}_{\mathcal{X}_0, \mathcal{E}, t} \left[\lambda(t) (s_{\theta_r} - \nabla_{\mathcal{R}} \log p_{t|0})^{\top} \Sigma_r (s_{\theta_r} - \nabla_{\mathcal{R}} \log p_{t|0}) \right], \quad (111)$$

where we omit arguments for brevity.

E.5.2 Substitution of the Score-Noise Identity. Using the Heteroscedastic Score-Noise Identity derived in Appendix E.3, we substitute the score terms with their noise counterparts:

$$s_{\theta_r} = -\frac{\Sigma_r^{-1} \boldsymbol{\varepsilon}_{\theta_r}}{\sqrt{1 - \bar{\alpha}_t}}, \quad \nabla_{\mathcal{R}} \log p_{t|0} = -\frac{\Sigma_r^{-1} \boldsymbol{\varepsilon}_r}{\sqrt{1 - \bar{\alpha}_t}}. \quad (112)$$

Plugging these into the loss function:

$$\begin{aligned} \mathcal{L}_{\text{real}}^{\text{cont}}(\theta_r) &= \mathbb{E}_{\mathcal{X}_0, \mathcal{E}, t} \left[\lambda(t) \left(-\frac{\Sigma_r^{-1}(\boldsymbol{\varepsilon}_{\theta_r} - \boldsymbol{\varepsilon}_r)}{\sqrt{1 - \bar{\alpha}_t}} \right)^\top \Sigma_r \left(-\frac{\Sigma_r^{-1}(\boldsymbol{\varepsilon}_{\theta_r} - \boldsymbol{\varepsilon}_r)}{\sqrt{1 - \bar{\alpha}_t}} \right) \right] \\ &= \mathbb{E}_{\mathcal{X}_0, \mathcal{E}, t} \left[\frac{\lambda(t)}{1 - \bar{\alpha}_t} (\boldsymbol{\varepsilon}_{\theta_r} - \boldsymbol{\varepsilon}_r)^\top \underbrace{(\Sigma_r^{-1})^\top \Sigma_r \Sigma_r^{-1}}_{\text{Matrix Simplification}} (\boldsymbol{\varepsilon}_{\theta_r} - \boldsymbol{\varepsilon}_r) \right]. \end{aligned} \quad (113)$$

E.5.3 Matrix and Coefficient Simplification. Since the spectral covariance matrix Σ_r is symmetric and positive definite, $(\Sigma_r^{-1})^\top = \Sigma_r^{-1}$. The central matrix term simplifies algebraically:

$$(\Sigma_r^{-1})^\top \Sigma_r \Sigma_r^{-1} = \Sigma_r^{-1} (\Sigma_r \Sigma_r^{-1}) = \Sigma_r^{-1} \mathbf{I} = \Sigma_r^{-1}. \quad (114)$$

Furthermore, to align the weighting with standard diffusion models, we set the SDE weighting function $\lambda(t)$ such that:

$$\frac{\lambda(t)}{1 - \bar{\alpha}_t} = \lambda_t \implies \lambda(t) = \lambda_t (1 - \bar{\alpha}_t). \quad (115)$$

Substituting the simplified matrix and coefficient back, we arrive at:

$$\begin{aligned} \mathcal{L}_{\text{real}}^{\text{cont}}(\theta_r) &= \mathbb{E}_{\mathcal{X}_0, \mathcal{E}, t} \left[\lambda_t (\boldsymbol{\varepsilon}_{\theta_r} - \boldsymbol{\varepsilon}_r)^\top \Sigma_r^{-1} (\boldsymbol{\varepsilon}_{\theta_r} - \boldsymbol{\varepsilon}_r) \right] \\ &= \mathbb{E}_{\mathcal{X}_0, \mathcal{E}, t} \left[\lambda_t \left\| \boldsymbol{\varepsilon}_{\theta_r}(\mathcal{R}, h(\mathcal{I}), t) - \boldsymbol{\varepsilon}_r \right\|_{\Sigma_r^{-1}}^2 \right] \\ &= \mathcal{L}_{\text{real}}^{\text{disc}}(\theta_r). \end{aligned} \quad (116)$$

The derivation for the imaginary component $\mathcal{L}_{\text{imag}}^{\text{cont}}(\theta_i)$ follows an identical path using Σ_i . This proves that minimizing the continuous-time score matching objective with the Mahalanobis norm is mathematically equivalent to minimizing the discrete-time noise prediction error weighted by the spectral precision matrix.

F Mathematical Lemmas

Lemma F.1. (Expectation of Product of Gaussian Noise Variables). Let $\{\epsilon_\tau\}$ be a sequence of independent and identically distributed (i.i.d.) Gaussian random variables, where $\epsilon_\tau \sim \mathcal{N}(\mu, \sigma^2)$. The expectation of the product of any two variables ϵ_n and ϵ_m is given by:

$$\begin{aligned} \mathbb{E}[\epsilon_n \epsilon_m] &= \begin{cases} \mathbb{E}[\epsilon_n^2], & \text{if } n = m \\ \mathbb{E}[\epsilon_n] \mathbb{E}[\epsilon_m], & \text{if } n \neq m \end{cases} \\ &= \mu^2 + \sigma^2 \delta_{n,m} \end{aligned} \quad (117)$$

where $\delta_{n,m}$ denotes the Kronecker delta function, defined as $\delta_{n,m} = 1$ if $n = m$ and 0 otherwise.

Lemma F.2. (Discrete Orthogonality of Trigonometric Basis). For any positive integer $T \in \mathbb{Z}^+$ and arbitrary integer $k \in \mathbb{Z}$, the discrete summation of cosine and sine functions over a full period T satisfies the following orthogonality properties:

$$S_{\cos}(k) = \sum_{\tau=1}^T \cos\left(\frac{2\pi k \tau}{T}\right) = T \cdot \delta_{k \bmod T, 0} \quad (118)$$

$$S_{\sin}(k) = \sum_{\tau=1}^T \sin\left(\frac{2\pi k \tau}{T}\right) = 0 \quad (119)$$

where $\delta_{i,j}$ is the Kronecker delta, and the condition $k \bmod T = 0$ implies that k is an integer multiple of T .

Proof.

By **Euler's Formula** $\exp(j\theta) = \cos \theta + j \sin \theta$, we construct the complex exponential sum $S(k)$:

$$S(k) = \sum_{\tau=1}^T \exp\left(j \frac{2\pi k \tau}{T}\right) = S_{\cos}(k) + j S_{\sin}(k). \quad (120)$$

Let $\omega_k = \exp\left(j \frac{2\pi k}{T}\right)$ denote the complex root of unity. The sum $S(k)$ forms a geometric series with common ratio ω_k :

$$S(k) = \sum_{\tau=1}^T (\omega_k)^\tau. \quad (121)$$

We evaluate this sum in two cases:

Case 1: Resonance (k is a multiple of T). If $k \equiv 0 \pmod{T}$, then $\frac{k}{T}$ is an integer, implying $\omega_k = \exp(j2\pi n) = 1$ for some integer n . The summation becomes a sum of ones:

$$S(k) = \sum_{\tau=1}^T 1 = T. \quad (122)$$

Equating real and imaginary parts gives:

$$S_{\cos}(k) = T, \quad S_{\sin}(k) = 0. \quad (123)$$

Case 2: Orthogonality (k is not a multiple of T). If $k \not\equiv 0 \pmod{T}$, then $\omega_k \neq 1$. Using the closed-form formula for a finite geometric series:

$$S(k) = \omega_k \frac{1 - (\omega_k)^T}{1 - \omega_k}. \quad (124)$$

Analyze the numerator term $(\omega_k)^T$:

$$(\omega_k)^T = \left[\exp\left(j \frac{2\pi k}{T}\right) \right]^T = \exp(j2\pi k) = 1. \quad (125)$$

Since k is an integer, the numerator $1 - (\omega_k)^T = 1 - 1 = 0$. Since the denominator $1 - \omega_k \neq 0$ (as $\omega_k \neq 1$), the total sum vanishes:

$$S(k) = 0. \quad (126)$$

This implies both real and imaginary parts are zero:

$$S_{\cos}(k) = 0, \quad S_{\sin}(k) = 0. \quad (127)$$

Conclusion. Combining both cases using the indicator function $\delta_{k \bmod T, 0}$, we obtain the stated results:

$$S_{\cos}(k) = T \cdot \delta_{k \bmod T, 0}, \quad S_{\sin}(k) = 0. \quad (128)$$

Q.E.D.

G Experimental Results

Models	Cont.	Disc.	Diff-TS	TimeVAE	TimeGAN	DDPM	
Context-FID	24	0.015\pm.001	0.018\pm.002	0.140 \pm .009	0.786 \pm .075	7.561 \pm 1.163	0.311 \pm .321
	64	0.053\pm.004	0.077\pm.005	0.273 \pm .033	0.856 \pm .227	9.266 \pm .860	0.438 \pm .123
	128	0.149\pm.006	0.175\pm.009	1.144 \pm .080	0.929 \pm .046	17.438 \pm 2.269	0.577 \pm .085
	256	0.591\pm.069	0.591\pm.069	2.152 \pm .092	1.025 \pm .080	28.819 \pm 2.444	0.899\pm.237
	Avg	0.202	0.215	0.927	0.899	15.771	0.556
Correlational	24	0.033\pm.023	0.044 \pm .014	0.066 \pm .016	0.103 \pm .028	1.482 \pm .007	0.032\pm.008
	64	0.045 \pm .012	0.040\pm.005	0.069 \pm .016	0.075 \pm .020	1.183 \pm .020	0.039\pm.016
	128	0.044\pm.006	0.053\pm.019	0.089 \pm .015	0.066 \pm .031	1.616 \pm .007	0.053\pm.034
	256	0.040\pm.008	0.057 \pm .016	0.119 \pm .009	0.045 \pm .012	1.480 \pm .008	0.044\pm.019
	Avg	0.041	0.049	0.086	0.072	1.440	0.042
Discriminative	24	0.008\pm.006	0.004\pm.004	0.073 \pm .016	0.167 \pm .138	0.445 \pm .087	0.066 \pm .142
	64	0.022\pm.007	0.032\pm.020	0.077 \pm .007	0.167 \pm .106	0.456 \pm .041	0.203 \pm .066
	128	0.038\pm.035	0.094\pm.066	0.171 \pm .016	0.169 \pm .141	0.414 \pm .158	0.198 \pm .382
	256	0.227 \pm .041	0.216 \pm .119	0.222 \pm .008	0.199\pm.130	0.437 \pm .073	0.084\pm.210
	Avg	0.074	0.087	0.136	0.176	0.438	0.138
Predictive	24	0.100\pm.004	0.119 \pm .004	0.118\pm.005	0.128 \pm .003	0.199 \pm .031	0.119 \pm .001
	64	0.114\pm.005	0.116\pm.008	0.117 \pm .003	0.118 \pm .002	0.151 \pm .007	0.120 \pm .011
	128	0.113\pm.009	0.108\pm.013	0.115 \pm .007	0.119 \pm .006	0.144 \pm .008	0.108\pm.004
	256	0.102\pm.015	0.105\pm.008	0.119 \pm .009	0.112 \pm .004	0.149 \pm .009	0.115 \pm .016
	Avg	0.107	0.112	0.117	0.119	0.161	0.116

Table 6: Unconditional Generation on ETTh1 Dataset. **Bold** and **underline** denote best and second best results.

Models	Cont.	Disc.	Diff-TS	TimeVAE	TimeGAN	DDPM	
Context-FID	24	0.022\pm.006	0.006\pm.001	0.187 \pm .021	0.190 \pm .043	1.739 \pm .558	0.025 \pm .004
	64	0.096 \pm .014	0.032\pm.012	0.424 \pm .026	0.371 \pm .076	2.143 \pm .448	0.093\pm.042
	128	0.413 \pm .045	0.338\pm.072	0.599 \pm .122	0.523 \pm .076	3.496 \pm .548	0.378\pm.140
	256	0.556 \pm .141	0.459\pm.146	0.532 \pm .071	0.286\pm.066	4.578 \pm 1.583	2.046 \pm .556
	Avg	0.272	0.209	0.436	0.343	2.989	0.636
Correlational	24	0.004\pm.003	0.006\pm.007	0.007 \pm .006	0.107 \pm .006	0.223 \pm .003	0.004\pm.004
	64	0.009\pm.005	0.011 \pm .007	0.014 \pm .004	0.093 \pm .006	0.218 \pm .005	0.003\pm.004
	128	0.014\pm.004	0.007\pm.003	0.020 \pm .006	0.087 \pm .001	0.217 \pm .005	0.015 \pm .004
	256	0.018 \pm .004	0.008\pm.008	0.009\pm.005	0.062 \pm .007	0.760 \pm .004	0.021 \pm .015
	Avg	0.011	0.008	0.013	0.087	0.355	0.011
Discriminative	24	0.014\pm.011	0.015\pm.021	0.086 \pm .007	0.100 \pm .075	0.459 \pm .021	0.108 \pm .179
	64	0.016\pm.013	0.046\pm.010	0.081 \pm .029	0.149 \pm .099	0.315 \pm .059	0.222 \pm .003
	128	0.061\pm.017	0.118\pm.051	0.122 \pm .006	0.127 \pm .144	0.196 \pm .141	0.204 \pm .134
	256	0.173 \pm .008	0.064\pm.010	0.134\pm.020	0.139 \pm .159	0.397 \pm .151	0.244 \pm .274
	Avg	0.066	0.061	0.106	0.129	0.342	0.195
Predictive	24	0.037\pm.000	0.037\pm.000	0.037\pm.000	0.040\pm.000	0.061 \pm .001	0.039 \pm .001
	64	0.037\pm.000	0.036\pm.000	0.037\pm.000	0.038 \pm .000	0.043 \pm .001	0.042 \pm .001
	128	0.037\pm.000	0.041 \pm .000	0.036\pm.000	0.037\pm.000	0.050 \pm .002	0.041 \pm .001
	256	0.037 \pm .000	0.038 \pm .000	0.036\pm.000	0.035\pm.002	0.099 \pm .035	0.044 \pm .000
	Avg	0.037	0.038	0.037	0.038	0.063	0.042

Table 7: Unconditional Generation on Stocks Dataset. **Bold** and **underline** denote best and second best results.

Models	Cont.	Disc.	Diff-TS	TimeVAE	TimeGAN	DDPM	
Context-FID	24	<u>0.007\pm.001</u>	<u>0.003\pm.001</u>	0.009 \pm .002	0.291 \pm .004	0.063 \pm .005	0.011 \pm .004
	64	<u>0.012\pm.002</u>	<u>0.018\pm.003</u>	0.029 \pm .004	1.263 \pm .069	1.392 \pm .065	0.038 \pm .010
	128	<u>0.043\pm.002</u>	<u>0.062\pm.005</u>	0.113 \pm .025	0.810 \pm .120	15.224 \pm .698	0.070 \pm .023
	256	<u>0.213\pm.022</u>	0.317 \pm .014	0.442 \pm .030	0.556 \pm .078	26.385 \pm 1.266	0.163\pm.046
	Avg	0.069	0.100	0.148	0.730	10.766	<u>0.071</u>
Correlational	24	0.026 \pm .011	<u>0.019\pm.006</u>	0.035 \pm .012	0.035 \pm .008	0.041 \pm .009	<u>0.021\pm.015</u>
	64	<u>0.023\pm.007</u>	<u>0.030\pm.010</u>	<u>0.023\pm.009</u>	0.165 \pm .011	0.137 \pm .010	<u>0.030\pm.004</u>
	128	<u>0.017\pm.004</u>	0.021 \pm .003	0.040 \pm .009	0.093 \pm .009	0.858 \pm .009	<u>0.019\pm.004</u>
	256	<u>0.011\pm.005</u>	0.015 \pm .004	0.021 \pm .005	0.050 \pm .007	0.918 \pm .005	<u>0.012\pm.007</u>
	Avg	0.019	<u>0.021</u>	0.030	0.086	0.489	<u>0.021</u>
Discriminative	24	0.008 \pm .004	<u>0.007\pm.008</u>	<u>0.006\pm.006</u>	0.021 \pm .020	0.020 \pm .013	0.012 \pm .009
	64	<u>0.008\pm.005</u>	<u>0.010\pm.003</u>	0.023 \pm .019	0.101 \pm .202	0.162 \pm .064	0.019 \pm .008
	128	<u>0.013\pm.016</u>	0.022 \pm .007	0.116 \pm .019	<u>0.019\pm.009</u>	0.477 \pm .019	0.027 \pm .041
	256	0.027 \pm .006	<u>0.023\pm.019</u>	0.163 \pm .105	0.130 \pm .214	0.378 \pm .263	0.011\pm.013
	Avg	0.014	<u>0.016</u>	0.077	0.068	0.259	0.017
Predictive	24	<u>0.093\pm.000</u>	<u>0.093\pm.000</u>	<u>0.093\pm.001</u>	0.227 \pm .000	<u>0.095\pm.001</u>	<u>0.093\pm.000</u>
	64	<u>0.188\pm.003</u>	<u>0.191\pm.002</u>	0.193 \pm .001	0.213 \pm .001	0.217 \pm .005	0.188\pm.007
	128	<u>0.252\pm.003</u>	<u>0.252\pm.003</u>	0.257 \pm .003	0.264 \pm .002	0.279 \pm .008	<u>0.255\pm.001</u>
	256	<u>0.286\pm.003</u>	<u>0.287\pm.003</u>	0.288 \pm .003	0.292 \pm .003	0.328 \pm .014	0.288 \pm .003
	Avg	0.205	<u>0.206</u>	0.208	0.249	0.230	<u>0.206</u>

Table 8: Unconditional Generation on Sines Dataset. **Bold** and underline denote best and second best results.

Models	Cont.	Disc.	Diff-TS	TimeVAE	TimeGAN	DDPM	
Context-FID	24	<u>0.026\pm.001</u>	<u>0.019\pm.001</u>	0.138 \pm .014	0.358 \pm .023	4.864 \pm .989	0.043 \pm .011
	64	<u>0.024\pm.002</u>	<u>0.065\pm.002</u>	0.387 \pm .023	0.460 \pm .021	10.320 \pm .487	0.284 \pm .053
	128	<u>0.122\pm.007</u>	0.421 \pm .034	<u>0.340\pm.031</u>	1.634 \pm .117	14.022 \pm 1.376	0.853 \pm .136
	256	<u>1.183\pm.052</u>	<u>1.575\pm.076</u>	0.723 \pm .057	3.200 \pm .134	24.603 \pm 1.898	1.230 \pm .369
	Avg	0.339	0.520	<u>0.397</u>	1.413	13.452	0.603
Correlational	24	<u>0.123\pm.058</u>	<u>0.115\pm.036</u>	0.163 \pm .035	0.358 \pm .026	0.494 \pm .008	0.170 \pm .077
	64	<u>0.068\pm.022</u>	<u>0.111\pm.032</u>	0.202 \pm .047	0.298 \pm .059	0.776 \pm .003	0.184 \pm .044
	128	<u>0.091\pm.027</u>	<u>0.091\pm.033</u>	<u>0.179\pm.028</u>	0.330 \pm .020	0.862 \pm .005	0.250 \pm .054
	256	0.256 \pm .038	<u>0.194\pm.046</u>	0.235 \pm .030	<u>0.229\pm.047</u>	0.916 \pm .005	0.332 \pm .054
	Avg	<u>0.135</u>	0.128	0.195	0.304	0.762	0.234
Discriminative	24	0.065 \pm .014	<u>0.036\pm.018</u>	0.072 \pm .012	0.391 \pm .034	0.432 \pm .144	<u>0.064\pm.015</u>
	64	<u>0.014\pm.012</u>	0.182 \pm .054	<u>0.125\pm.015</u>	0.389 \pm .026	0.355 \pm .135	0.142 \pm .064
	128	0.256 \pm .151	0.455 \pm .011	<u>0.160\pm.013</u>	0.442 \pm .010	0.473 \pm .011	<u>0.238\pm.058</u>
	256	0.484 \pm .010	0.448 \pm .026	<u>0.274\pm.098</u>	0.462 \pm .016	0.434 \pm .151	<u>0.364\pm.095</u>
	Avg	0.205	0.280	0.158	0.421	0.424	<u>0.202</u>
Predictive	24	<u>0.020\pm.001</u>	<u>0.021\pm.001</u>	0.022 \pm .001	0.030 \pm .002	0.101 \pm .008	<u>0.021\pm.002</u>
	64	<u>0.019\pm.001</u>	<u>0.020\pm.001</u>	0.021 \pm .001	0.026 \pm .001	0.216 \pm .016	0.022 \pm .006
	128	<u>0.019\pm.000</u>	<u>0.021\pm.001</u>	<u>0.021\pm.001</u>	0.026 \pm .001	0.293 \pm .034	0.022 \pm .003
	256	<u>0.021\pm.000</u>	0.024 \pm .000	<u>0.021\pm.002</u>	0.029 \pm .001	0.357 \pm .008	<u>0.022\pm.006</u>
	Avg	0.020	0.022	<u>0.021</u>	0.028	0.242	0.022

Table 9: Unconditional Generation on Air Quality Dataset. **Bold** and underline denote best and second best results.